Electropolymerization of Polydopamine at Electrode-Supported Insulating Mesoporous Films

Published as part of the Chemistry of Materials virtual special issue "In Honor of Prof. Clement Sanchez".

H. Samet Varol,*,[⊥] Tilmann Herberger,[⊥] Marius Kirsch, Joanna Mikolei, Lothar Veith, Venkataprasanna Kannan-Sampathkumar, Raoul D. Brand, Christopher V. Synatschke, Tanja Weil, and Annette Andrieu-Brunsen*

Read Online

ACCESS | Metrics & More | Article Recommendations | SI Supporting Information

ABSTRACT: Bioinspired, stimuli-responsive, polymer-functionalized mesoporous films are promising platforms for precisely regulating nanopore transport toward applications in water management, iontronics, catalysis, sensing, drug delivery, or energy conversion. Nanopore technologies still require new, facile, and effective nanopore functionalization with multi- and stimuli-responsive polymers to reach these complicated application targets. In recent years, zwitterionic and multifunctional polydopamine (PDA) films deposited on planar surfaces by electropolymerization have helped surfaces respond to various external stimuli such as

light, temperature, moisture, and pH. However, PDA has not been used to functionalize nanoporous films, where the PDA-coating could locally regulate the ionic nanopore transport. This study investigates the electropolymerization of homogeneous thin PDA films to functionalize nanopores of mesoporous silica films. We investigate the effect of different mesoporous film structures and the number of electropolymerization cycles on the presence of PDA at mesopores and mesoporous film surfaces. Our spectroscopic, microscopic, and electrochemical analysis reveals that the amount and location (pores and surface) of deposited PDA at mesoporous films is related to the combination of the number of electropolymerization cycles and the mesoporous film thickness and pore size. In view of the application of the proposed PDA-functionalized mesoporous films in areas requiring ion transport control, we studied the ion nanopore transport of the films by cyclic voltammetry. We realized that the amount of PDA in the nanopores helps to limit the overall ionic transport, while the pH-dependent transport mechanism of pristine silica films remains unchanged. It was found that (i) the pH-dependent deprotonation of PDA and silica walls and (ii) the insulation of the indium-tin oxide (ITO) surface by increasing the amount of PDA within the mesoporous silica film affect the ionic nanopore transport.
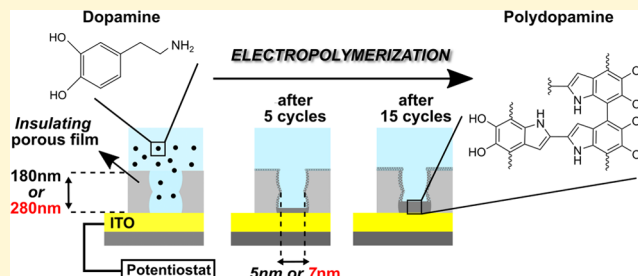
INTRODUCTION

The performance of the biological ion channels and pores is the key to survival for many living species.[1,2] Their precise mass transport control inspired scientists to build novel porous materials for challenging applications such as water purification,[3−5] energy conversion,[6−8] and molecular sensing.[9,10] One promising technology for mimicking these biological nanogates is ceramic mesoporous films functionalized by stimuli-responsive synthetic units at their pore sites. Mesoporous silica films have received significant attention among solid-state nanoporous films, thanks to their facile fabrication method and silanol-rich surface groups, making them easily adaptable for various chemical functionalization techniques. With the large number and small size of nanopores in the range of the hydrated radius of ions, mesoporous silica films are a versatile platform to regulate ionic nanopore transport after pore functionalization. After forming or attaching various stimuli-responsive polymer units in their nanopores in a controlled

amount, at a defined location, and with tailored stimuli-responsive units, these hybrid mesoporous films could be suitable for applications such as sensing or separation.[11] Recent examples showed that compared to pristine silica nanopores, similar pores with stimuli-responsive polymer units show significant improvements in various material properties such as sensing the nanomolar concentration of ions with memory effect,[12] ion concentration regulation such as electrokinetic ion transport,[13] or gradual control of ionic pore accessibility.[14,15] However, many of these polymer functionalization strategies of nanopores remain challenging to implement (e.g., multistep
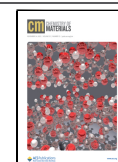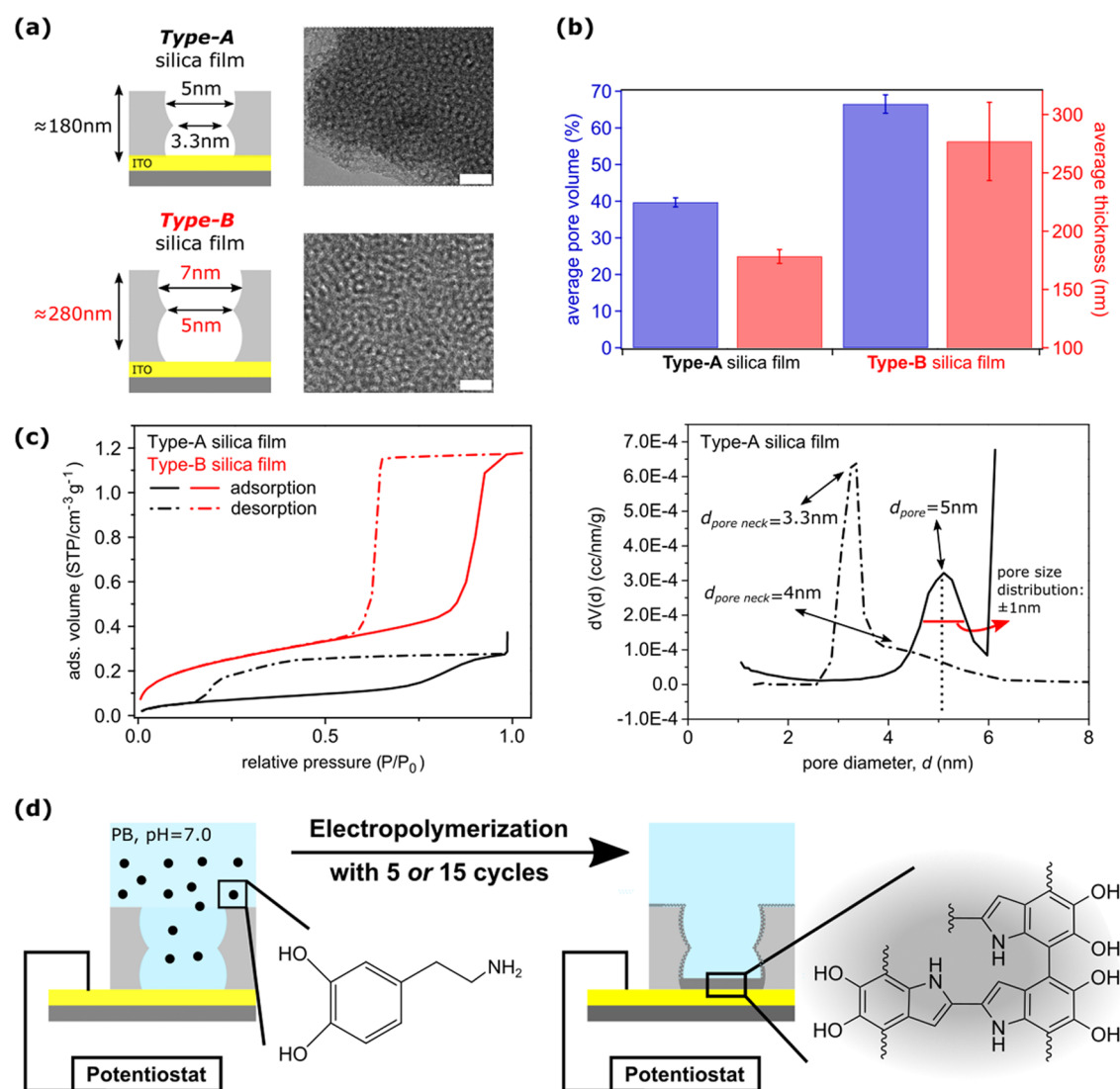
Figure 1. Mesoporous films and polydopamine (PDA) nanopore functionalization. (a) Illustrations presenting the film structure of (top) type-A and (bottom) type-B mesoporous films standing on top of the conductive indium-tin oxide (ITO) layer. Transmission electron microscopy images of type-A (up) and type-B (bottom) pore films are presented next to the corresponding illustrations. Scale bars are 50 nm. (b) Ellipsometry results present our mesoporous films' average free pore volume (blue bars and axis) and thickness (red bars and axis) before their PDA functionalization. Error bars represent the standard deviation (sd) from a minimum of three different measurements from the same sample. (c) (Left) Isotherms for type-A and type-B films obtained by Krypton 87.4 K physisorption as well as (right) the corresponding pore size and pore neck size distribution for the type-A film obtained by the Krypton thin-film (solid line) and BJH method (dashed line). (d) Scheme of our electropolymerization setup, showing the mesoporous films dipped inside the phosphate buffer (PB) solution loaded with dopamine (1 mg/1 mL) and the pH = 7.0. Upon 5 or 15 cycles of applied potential cycles to the ITO layer underneath our mesoporous films, electropolymerization of PDA happens at the film/ITO interface. The structure of PDA is simplified. The true structure of PDA is not finally elucidated to this day. Investigations of PDA's structure in the literature[55,56] led to the conclusion that various functional groups, such as amines, carboxylic acids, and phenolic hydroxyl groups are present in PDA.[57,58].

synthesis protocols) and provide limited functionality to the nanopores, e.g., by only charging positively or negatively under changing pH conditions or requiring additional pore functionalities to regulate other ion transport tasks. Therefore, research on the functionalization of nanopores with polymers continues to seek new, straightforward methods to fabricate nanopore films with zwitterionic polymer functionalities and smart-gating.

Due to the precise tunability of the surface polymerization process, electropolymerization represents an interesting method for generating functionalized nanoporous layers. Compared to conventional functional polymer thin-film deposition techniques, such as dip-coating, spin-coating, or inkjet printing, for specific coating applications, especially at biological interfaces, polymer deposition on conductive surfaces by electropolymerization offers several advantages.[16−18] For instance, by controlling the consumed charges during electropolymerization via an adjustment of the time and number of applied potential cycles, it is possible to achieve nanometer-level precision of the homogeneous polymer-coating.[19,20] Electrochemical polymer deposition also allows for spatially controlled deposition and creation of polymer patterns on various surfaces, for instance, to build patterned thin-film transistors.[21−23] While conventional polymerization methods, such as dip-coating, usually take several hours to form stable polymer-coatings, film deposition via electro-

polymerization is a very fast method to form uniform polymer films within seconds.[24,25] For decades, electropolymerization has been used to polymerize predominantly aromatic monomers, such as furan, pyrrole, or aniline, to form various types of conductive polymer-coatings on the solid-state electrode surface.[26−28] In recent years, electropolymerization was recognized as a suitable technique also for nonconducting monomers such as catecholamines, like dopamine. Polydopamine (PDA) films have raised considerable interest as versatile coating materials. Multifunctionality, high stability, and simple but finely tunable nanofilm deposition on various materials (metals, ceramics, and plastics) via electropolymerization make PDA a suitable candidate for polymer functionalization for various applications.[18,19,29,30] PDA-coated materials can be easily chemically modified, for example, with catalytic centers[31] and biomolecules such as proteins[32] and nucleic acids.[33] To date, PDA-coatings find applications in catalysis,[34] biomedical,[30,35] sensing,[36] photonics,[37] and actuators.[38] The presence of various functional groups, such as amines, carboxylic acids, and phenolic hydroxyl groups makes PDA a versatile polyelectrolyte that changes its charge state in response to the pH, thereby affecting the transport of anions and cations.[39−42] The abovementioned structural features, simple fabrication, and its zwitterionic properties could make PDA an ideal polymer for applications requiring high-precision ionic transport control such as sequential transport[43] and drug delivery.[18] PDA's zwitterionic effects on ion transport were so far only used with planar PDA-coatings on conductive (e.g., gold layer) materials. This left only the PDA thickness and changing environmental pH as the parameters to tune transport. However, it would be highly interesting to study whether electropolymerization could be used to generate zwitterionic PDA at the nanopores of mesoporous silica films by combining the structural advantages of both PDA and mesoporous silica. To date, PDA nanopore functionalization has been demonstrated for mesoporous silica nanoparticles via multistep oxygen-induced surface functionalization. The combination of the large surface area of nanoparticles and pH-responsive structural advantages of PDA could make these PDA functional nanocarrier systems a useful platform for various applications such as load/release hydrophilic drugs.[44,45] However, PDA polymerizations in solution in the presence of chemical oxidants does not give control over the polymerization reaction and this leads to the formation of free PDA particles that are difficult to remove.[46] Electropolymerization of PDA offers high control of redox reactions on the electrode surface and thus the amount of deposited PDA at nanoconfinement of mesoporous films. In this way, homogeneous thin and more uniform PDA-coatings are generated in a fast and efficient manner and with precise control of the film thickness compared to other PDA polymerization methods.[32,46,47] The electropolymerization method allows to gradually tune the amount of PDA inside and on top of the nanopores of mesoporous silica films with zwitterionic PDA contributing to the technological advancement of ionic transport control in nanoporous membranes.

In this work, for the first time, we electropolymerized PDA inside two different types of mesoporous silica films that are nonconductive and nonplanar. The electropolymerization caused deposition of PDA on top of the indium-tin oxide (ITO) working electrode and inside and on top of the insulating mesoporous films. We demonstrated that the type of mesoporous silica film and the number of electropolymeriza-tion cycles alter the PDA deposition pattern. We identified the effect of these parameters on the amount of deposited PDA (i) at the pore sites, (ii) at the interface of mesoporous film/ITO where the polymerization takes place, as well as (iii) on the film surface. The adjustment of the amount and distribution of the polymer constitutes a toolbox for the regulation of nanopore performance. We evaluated the environmental pH-dependent nanopore transport of anions and cations through the PDA-coated mesoporous films. Ultimately, (i) PDA and silica pore walls' pH-dependent charging, (ii) changing the presence of PDA at the nanopore walls, and (iii) mesoporous film/ITO interface regulate together the ionic nanopore transport at our PDA functional mesoporous silica films.

RESULTS AND DISCUSSION

Electropolymerization of Polydopamine in Nanoconfinement. Electropolymerization of polydopamine (PDA) in nanoconfined silica mesopores was investigated by using two different mesoporous silica films having different nanopore and film structures—type-A and type-B mesoporous films (Figure 1). These two films were dip-coated on the top of indium-tin oxide (ITO)-coated glass substrates (Figure 1a). Similar to literature examples,[48,49] variations in the sol−gel solution recipe change the average free pore volume and film thickness of the dip-coated mesoporous films, as we quantified with ellipsometry measurements (Figure 1b). As presented in Figure 1b, our type-A film's average free pore volume (40 ± 1.2%) and film thickness (178 ± 6 nm) are smaller than those of the type-B film (67 ± 2.5%; 277 ± 34 nm). Krypton physisorption at 87.4 K was performed with type-A and type-B films to determine their pore size, pore size distribution, and pore neck size. At 87.4 K, the measurement is performed below the triple point of Krypton.[50] Because of measuring below the triple point, Krypton solidification can occur at high relative pressure, which results in a steep uptake of adsorption. This may be the reason for the steep uptake in the isotherm of the type-A silica film presented in Figure 1c-left (black isotherm). However, such Krypton solidification did not influence the derived pore size or pore size distribution from the isotherms (Figure 1c-right). For both type-A and type-B films, we collected isotherms that are characteristic for mesoporous materials (Figure 1c).[51] By applying the Krypton 87.4 K thin-film method to the collected isotherms, a pore size of 5 ± 1 nm for the type-A and 7 ± 1 nm for the type-B films was determined (Figures 1c-right and S1). Applying the Barrett−Joyner−Halenda (BJH) method to the desorption branch of the type-A film yields two values for the pore neck openings, 3.3 and 4 nm (Figure 1c-right). However, as shown in Figure 1c-right (dashed lines), the primary (peak with highest intensity) pore neck size calculated from a type-A film is 3.3 nm. These pore opening diameters are in good agreement with those calculated from the transmission electron microscopy (TEM) image analysis (3.2 ± 0.7 nm for type-A) by using an image thresholding routine (Figure S2).[52−54] With identical TEM image analysis, the pore neck opening of the type-B film is quantified as 5.0 ± 1.9 nm (Figures 1a and S2).

To perform electropolymerization in mesoporous films, type-A and type-B films were immersed into a solution of dopamine monomers in nitrogen-purged phosphate buffer (pH 7.0, 1 mg/mL dopamine). 5 or 15 potential cycles from −0.5 to 0.5 V were applied to the ITO/glass substrate (working electrode) located below the mesoporous silica films to initiate the electropolymerization via cyclic voltammetry (CV) at the
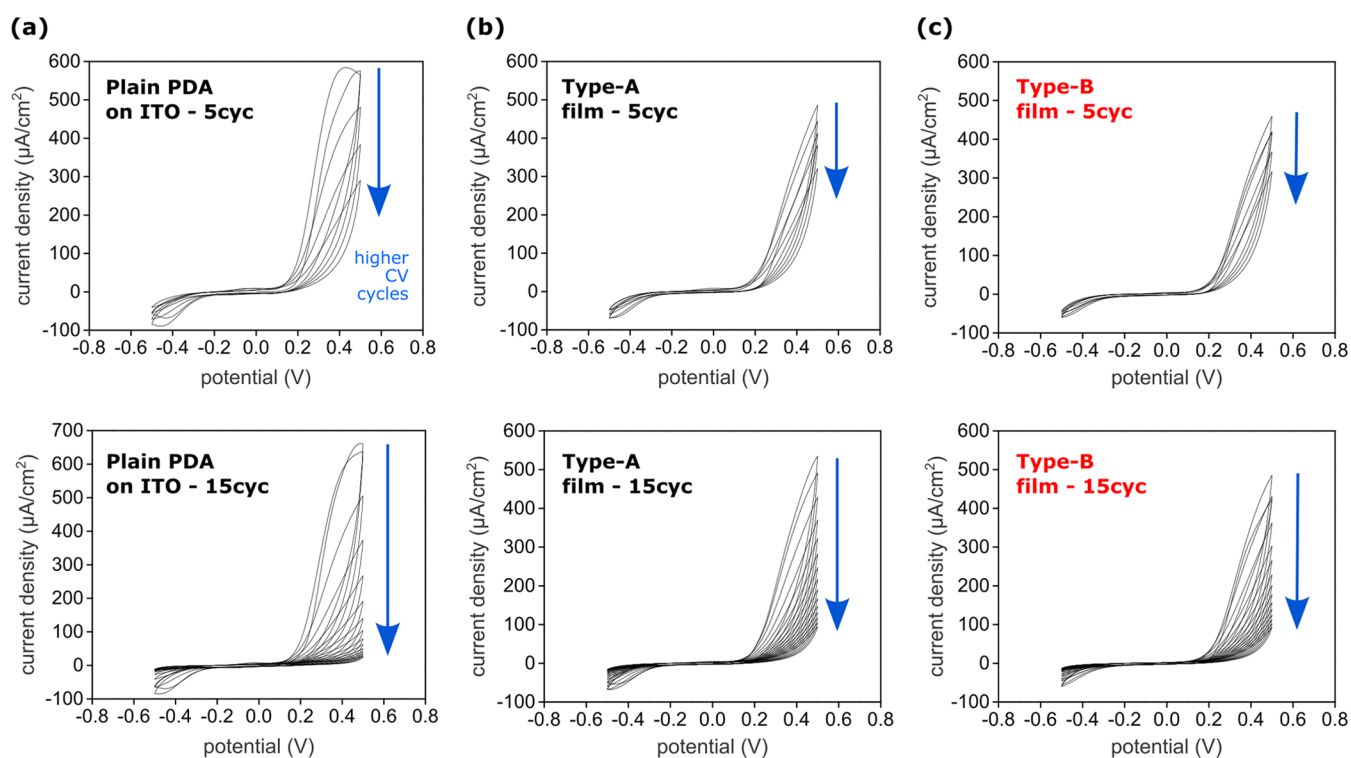
Figure 2. Cyclic voltammetry (CV) curves collected during (top) 5 cycles and (bottom) 15 cycles of electropolymerization of PDA when dopamine (1 mg/mL), dissolved in nitrogen-purged, oxygen-free phosphate buffer (100 mM, pH 7), is in contact with (a) planar ITO substrate (working electrode, no mesoporous film on the top) and (b) type-A or (c) type-B mesoporous films. The direction of the blue arrows indicates the decrease of the current throughout the CV cycle progression. Experiments were conducted at room temperature. An Ag/AgCl reference electrode (3 M KCl) and a gold counter electrode were used. A scan rate of 10 mV/s was applied.

vicinity of the ITO/mesoporous film interface (Figure 1d). The CV curves collected during the 5- and 15-cycle electropolymerization of PDA on the planar ITO (no mesoporous film on the top) and mesoporous film-coated ITO are shown in Figure 2. During our reference PDA electropolymerization on planar ITO (Figure 2a), the oxidative current decreased with the progression of the applied potential cycles during both the 5- and 15-cycle electropolymerization (blue arrows in Figure 2a). This decrease in current is caused by deposition of the insulating PDA on the ITO surface. As studied before by Marchesi D'Alvise et al., the degree to which the current decreases in an electropolymerization on gold correlates with the thickness of the deposited insulating PDA layer.[32] It can be assumed that this is also the case for electropolymerization on ITO. The reducing current also resembles the reduction of non−crosslinked redox−groups inside the polymer on the conductive surface. As PDA crosslinks more, when the number of cycles increases and the reductive current decreases, as shown in Figure 2a.

The fact that a substantial oxidative current can also be observed for the mesoporous film-covered samples (Figure 2b,c) shows that the insulating mesoporous silica membrane does not completely insulate the ITO electrode. Dopamine is still electrochemically oxidized, and PDA is formed. Similar to the polymerization on plain ITO, the current decreases throughout the progression of the cycle number (blue arrows in Figure 2b,c). The decrease in current indicates that PDA is not only present as particles that float inside the bulk solution and deposit on the surface of the silica membrane but also that it is deposited on the ITO surface of both type-A and type-B films. However, this decrease in the current is less intense at a

given current value and a given cycle for the mesoporous film carrying samples (Figure 2b,c) compared to plain ITO (Figure 2a). This indicates that less PDA is deposited on the ITO surfaces of these samples. Even after 15 cycles, the current is considerably high (100 μA/cm^2) for the silica film-covered samples (Figure 2b,c-bottom), while it is about 10 times lower (10 μA/cm^2) for the blank ITO (Figure 2a-bottom). The high current intensities during each of the single cycles, including the last one, indicate that a significant amount of PDA is formed but that only a small portion of it is deposited on the ITO surface. We assume that a substantial amount of PDA was dispersed in the bulk solution and deposited on top of the silica film and inside its pores. Interestingly, no large difference was detected between the CV curves collected during the polymerization of type-A and type-B films.

The oxidative part of the first CV voltammograms in Figure 2 shows a steeper increase of the oxidative current as a factor of increasing the applied potential. This is due to the decreased availability and accessibility of the ITO surface area for dopamine monomers when it is coated with a mesoporous membrane. We confirmed the limited electrode surface availability by analyzing the oxidation and reduction of potassium ferrocyanide on different sample types (Figure S3). Such a limitation of dopamine accessibility to ITO when mesoporous films are deposited on top of the ITO electrode is also made responsible for obtaining no oxidative peak in their CV curves (Figure 2b,c). The oxidative peak in the first cycles of the CV for the blank ITO (Figure 2a) is ascribed to the diffusion rate of dopamine monomers from the bulk solution to the ITO surface reaching its maximum, at which, an increase in voltage is not anymore correlated with an increase in current
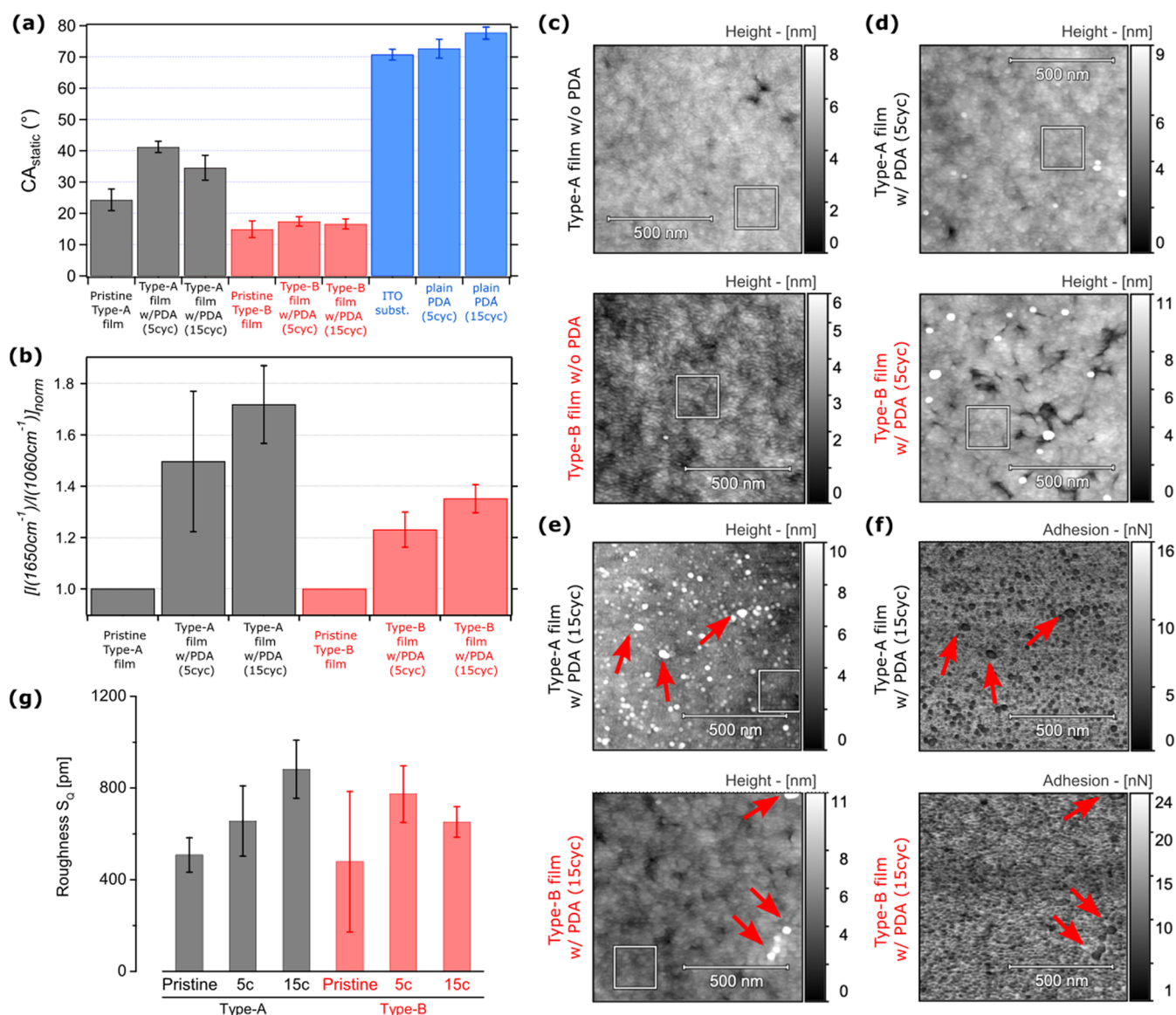
Figure 3. (a) Static contact angle (CA_{static}) of sessile drops on the top of (black) type-A and (red) type-B mesoporous films before and after different cycles of e-polymerization of PDA. The blue bars present the CA_{static} from the plain PDA films (no mesoporous film) on the top of the ITO substrate surface. Error bars represent the sd from CA_{static} collected from at least five different locations from the same sample. (b) Bar graph presenting the relative increase of the normalized (to the Si−O−Si vibration at 1060 cm^{-1}) ν_{ring}(C≡C) stretching mode and N−H bending mode vibration peaks (between 1600 and 1650 cm^{-1}) after the PDA functionalization of the porous films. Error bars represent the sd from a minimum of three different attenuated total reflection-infrared (ATR-IR) spectra collected from different locations of the same sample. (c, e) SFM topography images of our type-A and type-B pore films (on the top of ITO) (c) before and after (d) 5 cycles or (e) 15 cycles of e-polymerization of polydopamine. (f) Adhesion force mapping of the identical areas whose SFM topographies are presented in panel (e). Red arrows in panels (e) and (f) present weakly attached impurities. (g) Roughness (S_Q) values were generated from the 200 μm × 200 μm area SFM topographies (marked with white squares) from the larger-area images presented in panels (c−e) and Figures S9 and S10. Error bars represent the sd from the roughness measurements of three different 200 μm × 200 μm areas on each sample.

since the current generation is limited by the maximal amount of dopamine monomers at the ITO surface.[32] This maximum seems not to be reached for the mesoporous film-covered samples. This is probably due to slower oxidation. Furthermore, plain ITO (Figure 2a) allows for higher oxidative currents during electropolymerization than both mesoporous film-coated ITO substrates (Figure 2b,c). This indicates that dopamine oxidation inside the mesoporous films is limited.

Before (Figure S4, first and third rows) and after (Figure S4, second and fourth rows) the electropolymerization of our samples, we did further electrochemical analysis to understand the polymerization mechanism and stability of the deposited

PDA. We observed cathodic currents for some samples, which are due to the reduction of oxygen that diffuses into the electrolyte. We confirmed this diffusion and reduction of oxygen by analyzing oxygen reduction on pristine ITO in purged and nonpurged PB (Figure S5). As predicted, CV curves collected before the electropolymerization (Figure S4, first and third rows) did not form a peak at the anodic part since no polymerization occurred in the absence of dopamine in buffer solution. However, the CV curves collected after the PDA functionalization of our samples (Figure S4, second and fourth rows) showed the highest peak current in the first CV cycles, and this peak current decreases with increasing CV

cycle numbers. This analytically proves the successful deposition of PDA on the top of ITO both at our mesopore films coated on ITO and plain ITO. The decrease of the PDA peak throughout the cycle progression indicates that the supramolecular structure of PDA initially contains a significant number of free redox groups, which get electrochemically oxidized by the CV in pure PB and subsequently cross-link irreversibly. This observation motivated us to add additional CV cycles in pure buffer to the procedure that we established for the electropolymerization in nanoconfinement, so that the PDA does further cross-link (Figure S7b). The additional CV cycles ensure that the amount of noncovalently bound monomers and oligomers, which could potentially diffuse inside the pores and on the surface of the membrane, is minimized. This increases the reproducibility and controllability of the polymerization and confines deposition of PDA inside and on top of the membrane. Moreover, differential pulse voltammetry (DPV, Figure S6) measurements detect the cross-linked PDA on plain ITO as well as on ITO carrying type-A mesoporous film. The peaks in our DPV data after PDA polymerizations (Figure S6c,d) further demonstrate the presence of electrochemically accessible free redox groups of PDA. The observed voltage (0,18 V) for the PDA peak is reported for dopamine detection via DPV.[57] In general, the CV voltammograms collected during and after PDA electropolymerization (Figures 2 and S4) show that electropolymerization inside the mesopores was successful. Our electrochemical measurements after polymerization demonstrate the PDA deposition directly on ITO from our samples with or without mesoporous films. However, CVs collected during polymerization also indicate the possibility of PDA polymerization in solution. Moreover, these free PDA particles could deposit inside and on top of the membrane. To analyze localized PDA deposition inside and outside the nanopores, we characterized our samples with different surface wetting, spectroscopy, and scanning force microscopy (SFM) measurements as explained in the following sections.

Influence of the Mesoporous Film Structure on PDA Formation. After electropolymerization of PDA directly on the planar ITO substrate (no mesoporous film), we observed an increase in the static contact angle (CA_{static}) (blue bars in Figure 3a). CA_{static} of the non-PDA-coated ITO surface is $71 \pm 2°$ but CA_{static} increases to 73 ± 3 and $78 \pm 1°$ after 5 and 15 cycles of electropolymerization of plain PDA on ITO. This may indicate that in addition to the stronger deposition of the PDA film on the ITO surface, an increasing number of electropolymerization cycles might also lead to the formation of some PDA particles that can diffuse to the top of the mesoporous film surface and increase the surface hydrophobicity. CA_{static} of the pristine type-A mesoporous silica film ($CA_{static} = 24 \pm 3°$) increases to $CA_{static} = 41 \pm 2$ and $35 \pm 4°$ for 5 and 15 cycles of PDA functionalization, respectively. Also, for the type-B films ($CA_{static} = 15 \pm 3°$), upon 5 and 15 cycles of PDA functionalization, CA_{static} values slightly increased and recorded as $CA_{static} = 17 \pm 2°$ for both samples (red bars in Figure 3a). Larger PDA deposition-related CA_{static} increase in type-A films than in type-B films may indicate that when the mesoporous film is thin (type-A), large number of polymerized PDA might diffuse from the confining mesopores to the buffer electrolyte and afterward attach to the top of the film and increase the CA_{static}. For testing this hypothesis, CA_{static} of 5-cycle PDA-functionalized type-A and type-B films were checked before and after studying their ionic nanopore

transport by applying different numbers of potential cycles with different scan rates (see Experimental Section; see also Figures 5 and 6). After nanopore transport measurements using cyclic voltammetry, CA_{static} values were found as CA_{static} = 73 and 70° for the PDA-functionalized type-A and type-B films, respectively (Figure S8a—dot-patterned bars). After the ionic nanopore transport experiments, in addition to the possibility of PDA particle diffusion on the film surface, such a significant increase in CA_{static} probably was affected by other factors too, such as changes in the roughness of the PDA films and attachment of electroactive species (e.g., ionic probes and/or KCl) on the surface. Indeed, when we checked the CA_{static} of type-B films before and after applying extra potential cycles for cross-linking the PDA where no dopamine exists in the electrolyte (Figure S8a—line-patterned red bars), we did not see any significant change in CA_{static}. This suggests that the deposited PDA at the nanopores is quite stable and the effect of PDA attachment on the film surface on hydrophobicity is insignificant. Therefore, the significant increase in CA_{static} after studying the ionic nanopore transport is probably a combination of electroactive species attachment on the film surface and PDA roughness changes at the film surface. The stability of PDA at the nanopores was also observed from other supplementary results presenting the existence of PDA on the ITO surface after applying postpolymerization CV cycles (Figures S4 and S7) and after long incubations (21 h) in the electrolyte solution (Figure S8f).

To quantify the total amount of PDA at our mesopore films, we measured the films before and after their PDA functionalization at different number of CV cycles by attenuated total reflection-infrared (ATR-IR) spectroscopy (Figures 3b and S8b—d).[43,49,50] Figure 3b shows the normalized IR intensity of characteristic $\nu_{ring}(C=C)$ stretching mode and bending vibration of N—H peak (between 1600 and 1650 cm^{-1})[19,45,58] from PDA. First, the normalized intensity of the characteristic PDA peak between 1600 and 1650 cm^{-1} increases after 5 and 15 cycles of PDA functionalization of both type-A and type-B films due to having PDA at the vicinity (inside and outside of the pores) of both films. Moreover, this characteristic peak intensity further increases for both films with an increasing number (15 cycles) of PDA deposition cycles. This means that for both mesoporous films, it is possible to increase the PDA amount with an increasing number of electropolymerization cycles. To understand if PDA is located on the top of the mesoporous films after the electropolymerization, we investigated the surface topography of the mesoporous films before (Figure 3c) and after their 5-cycle (Figure 3d) or 15-cycle (Figure 3e,f) electropolymerization by scanning force microscopy (SFM). After the PDA functionalization, SFM height maps of mesoporous films (Figure 3d,e) showed some impurities (round-shaped and very bright) attached to the surfaces. The adhesion maps (Figures 3f, S9d,f, and S10d,f) and their corresponding height maps (Figures 3e, S9c,e, and S10c,e) showed that these deposits are less adhesive than the rest of the surface area (red arrows in Figures 3e,f, S9c—f, and S10c—f). This indicates that these weakly adhered impurities are likely not a part of polymerized PDA but potentially buffer salts or dirt deposits weakly attached on surfaces. Therefore, to exclude the impact of these bright impurities from the presented S_Q in Figure 3g, we derived S_Q from the impurity-free smaller areas inside larger SFM maps (white squares in Figure 3c—e). As presented in Figure 3g, the roughness increases for both mesoporous films
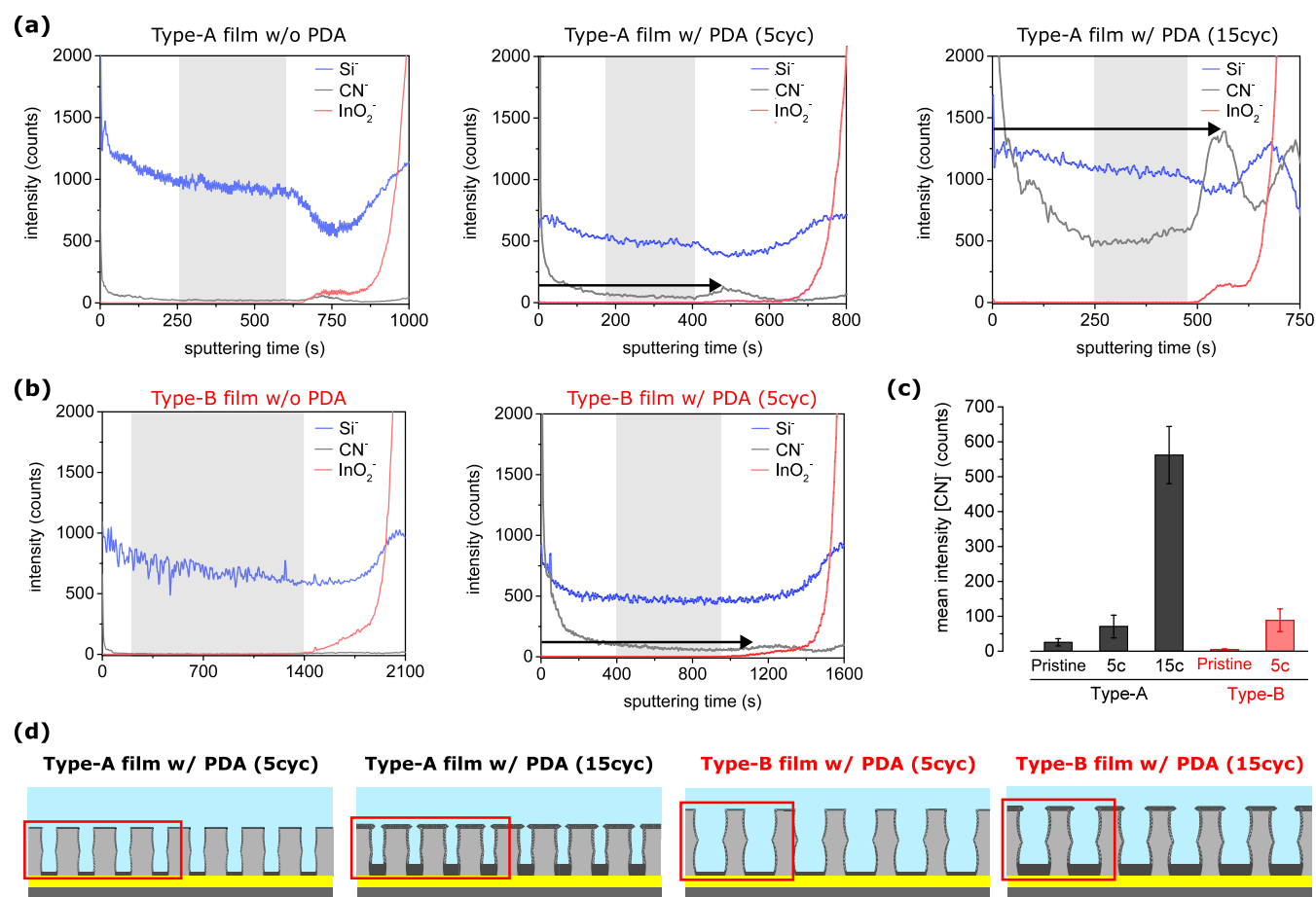
Figure 4. (a) Tof-SIMS depth profiling data of (left) pristine (no PDA), and PDA-functionalized type-A films after (middle) 5 and (right) 15 electropolymerization cycles. In panel (b), the ToF-SIMS depth profiles for (left) non-PDA-functionalized and (right) 5-cycle PDA-functionalized type-B films are presented. (a, b) Depth profiles show the ionic signals of Si^- (blue), CN^- (gray), and InO_2^- (red). The gray areas mark the middle section of the mesoporous film thickness (between ITO and air), and the arrows connect the local CN^- maxima detected at the silica film/ITO interface with the y-axis. (c) Average intensities of counted CN^- ions from each sample's middle section (gray areas in panels (a) and (b)). The error bars represent the sd from the average value by taking each of the measured data point, which are inside the gray area, into consideration. (d) Illustrations of type-A and type-B mesoporous films after their PDA functionalization with 5 and 15 cycles. PDA polymers were presented by dark gray color. Red boxes represent qualitatively similar areas of type-A and type-B films to help the reader imagine the amount of PDA at the nanopores.

after PDA functionalization. Additionally, for PDA-functionalized type-A films, it is evident that the increasing number of electropolymerization cycles also increases the roughness. For type-B samples, this correlation could not be observed. Such overall roughness increase upon PDA deposition indicates the formation of a PDA layer on top of the mesoporous silica film. One can furthermore visually observe in the height profiles in Figures 3, S9, and S10 that the surface profile of the membranes is less sharp for the PDA-coated samples, which indicates deposition of a thin PDA layer on the membrane surface. Furthermore, the adhesion measurements (Figures 3f, S9b,d,f, and S10b,d,f) show a higher adhesion (bright) for the surface area that is presumably coated by a PDA layer than for the weakly adhered depositions (dark) that are presumably buffer salts and dirt. To investigate the effect of the mesoporous film type and the number of electropolymerization cycles on the PDA deposition pattern, we analyzed our samples with time-of-flight secondary ion mass spectrometry (ToF-SIMS, Figure 4).

We characterized both the type-A and type-B mesoporous films before (Figure 4a,b-left) and after (Figure 4a-middle,b-right) their 5-cycle PDA functionalization and the type-A film

also after (Figure 4a-right) its 15-cycle PDA functionalization. Depth profiles of ablated ionic species are measured to characterize the localized PDA deposition along the mesoporous film thickness (Figure 4a,b). Blue, gray, and red data points represent ionic signals coming from mesoporous silica (Si^-), PDA (CN^-), and ITO (InO_2^-). The sample can be divided throughout its depth into three sections—the air/membrane interface, the middle section (gray), and the membrane/ITO interface. It must be noted that the sputtering time (x-axis of Figure 4a,b) is not linearly correlated with the mesoporous film depth since the speed of erosion may change throughout the sections of a sample and in between samples. Intensity points at very low sputtering time in Figure 4a,b that are collected at the membrane/air interface are excluded from interpretation since changes in the matrix at this interface may lead to strong matrix effects. The middle section (gray in Figure 4a,b) is characterized by the absence of drastic changes in ion signal intensities due to the establishment of a sputter equilibrium in a relatively constant matrix. Therefore, Figure 4c shows the mean intensities of the CN^- signals collected from the middle sections. The CN^- intensities for the pristine silica films indicate background signals of 22 (type-A) and 4 (type-
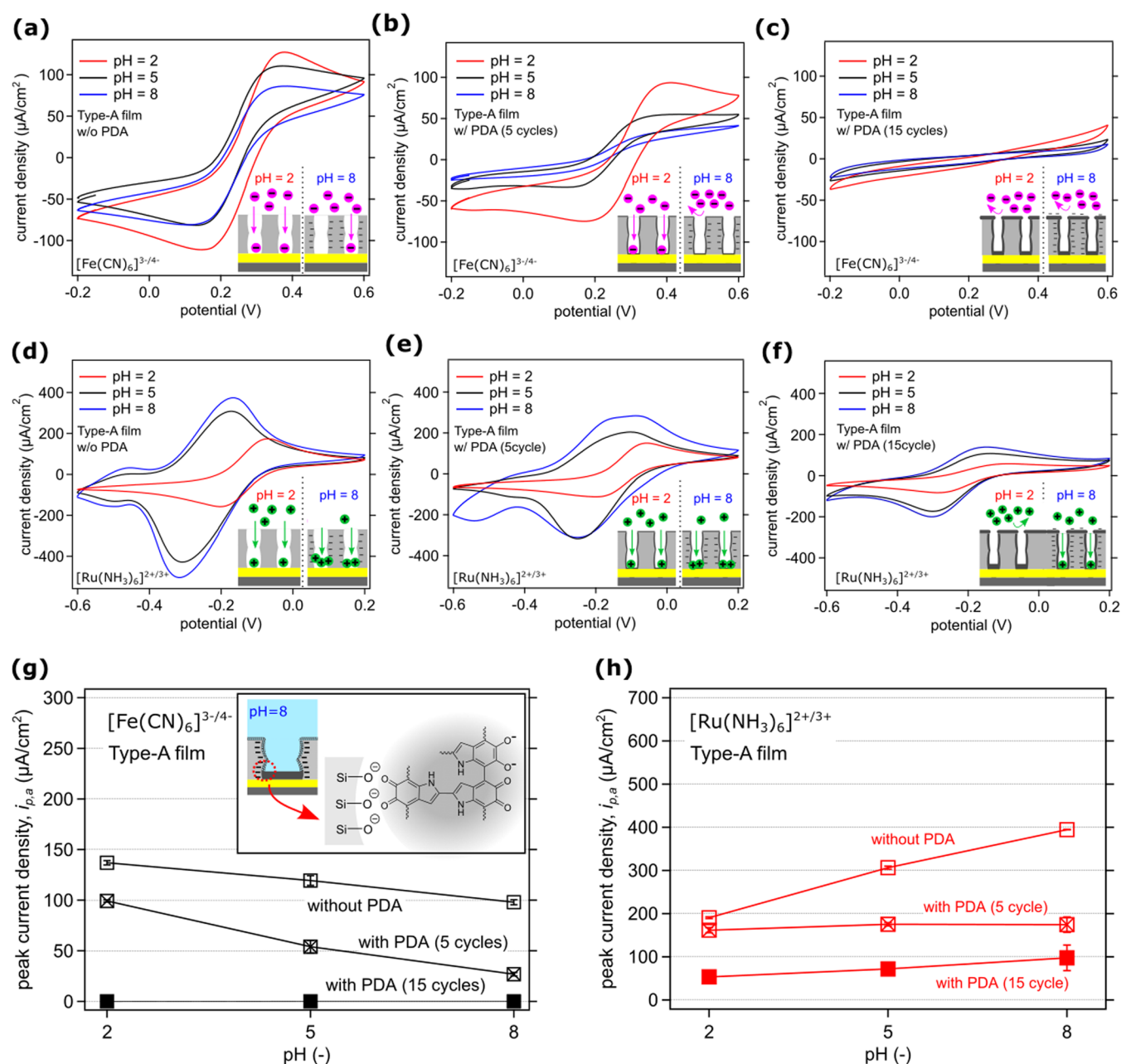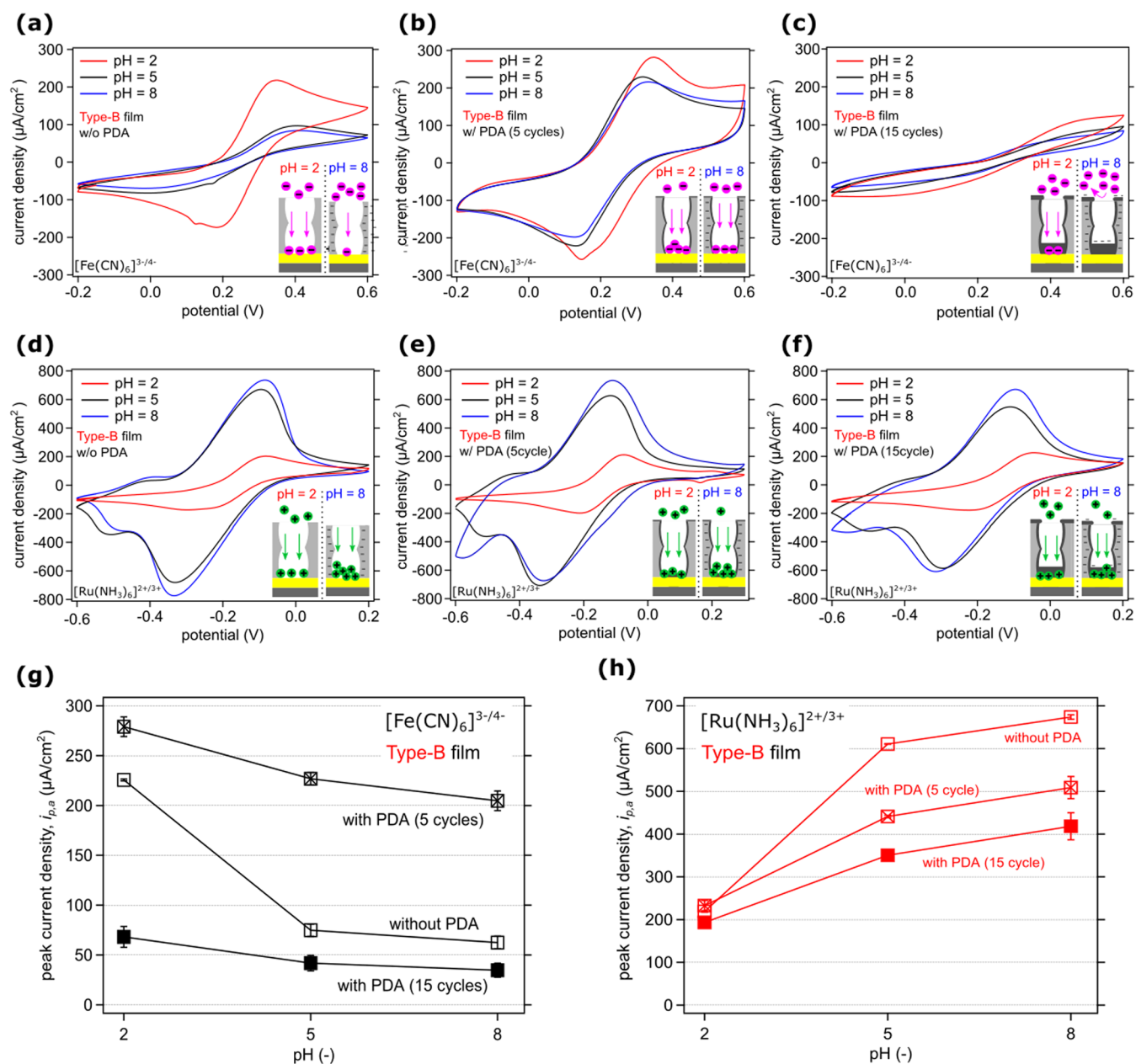
Figure 5. Cyclic voltammograms of type-A mesoporous silica films (a, d) before and (b, c, e, f) after PDA pore modification. CV curves presented in panels (b) and (e) and (c, f) were collected from the PDA-functionalized samples after 5 and 15 electropolymerization cycles, respectively. All measurements were performed at pH values of 2, 5, and 8. The transport through the pores was studied by using (a–c) $[Fe(CN)_6]^{3-/4-}$ and (d–f) $[Ru(NH_3)_6]^{2+/3+}$ as anionic and cationic redox probes, respectively. The scan rate used for all of the measurements was 200 mV/s, ionic probe concentrations were kept as 1 mM, and the electrolytes also included 100 mM KCl. Insets in panels (a–f) illustrate the ionic nanopore transport through the type-A mesopore films without and with PDA functionalization at pH values of (left) 2 and (right) 8. Anionic and cationic probes are shown as purple and green filled circles, respectively. The working electrode (ITO) and polydopamine are presented by yellow color bars and gray-color films, respectively. (g, h) Anodic peak current density ($i_{p,a}$, $\mu A/cm^2$) and electrolyte pH relation on (g) anionic (black, $[Fe(CN)_6]^{3-/4-}$) and (h) cationic (red, $[Ru(NH_3)_6]^{2+/3+}$) probe transport through PDA-functionalized or neat type-A silica films. Error bars are sd derived from a minimum three CV curves from measurements with a 200 mV/s scan rate. Inset in panel (g) illustrates the nanopores at alkaline pH conditions, where PDA and silica walls deprotonate.

B) counts, presumably caused by air adsorbents. The type-A film that is functionalized with PDA via 5 cycles produces considerably higher CN⁻ intensities (52 counts on average) than the nonfunctionalized type-A film, which resembles deposition of PDA inside the nanopores. The localized amount of PDA deposited on the ITO working electrode after 5 cycles is indicated by a local maximum of the CN⁻ intensity at 130 counts (arrow in Figure 4a). The 5-cycle PDA-functionalized

type-B film shows a similar deposition pattern, with 71 counts inside the pores and 100 counts at the local maximum on ITO. This is in good agreement with our ATR-IR results (Figure 3b). However, an increase in electropolymerization cycles (type-A (15 cycles)) increases the PDA deposition both at the pore walls (on average 562 counts) and at the film/ITO working electrode interface (1389 counts at a local maximum) significantly. Any change in the composition of a sample's

Figure 6. Cyclic voltammograms of type-B silica films (a, d) before and (b, c, e, f) after PDA pore modification after (b, e) 5 and (c, f) 15 electropolymerization cycles. The ionic nanopore transport was studied at pH 2, 5, or 8 and by using (a−c) $[Fe(CN)_6]^{3-/4-}$ as an anionic redox probe and (d−f) $[Ru(NH_3)_6]^{2+/3+}$ as a cationic redox probe. The scan rate for all of the measurements was 200 mV/s, the concentrations of the ionic probes in the electrolytes were 1 mM, and also 100 mM KCl was added into each electrolyte. Illustrations at the insets present the ionic nanopore transport at the type-B films with and without PDA functionalization when the bulk pH is (left) 2 or (right) 8. Gray areas show the polydopamine in the vicinity of the pores, and the working electrode ITO layer was sketched by a yellow bar under the films. Purple and green filled circles represent anionic and cationic probes, respectively. (g, h) Relation between anodic peak current density, $i_{p,a}$ (μA/cm^2), and solution pH from the CV curves in panels (a−f) to understand the transport of (g) anionic ($[Fe(CN)_6]^{3-/4-}$) and (h) cationic ($[Ru(NH_3)_6]^{2+/3+}$) redox probes inside type-B silica pores with or without PDA functionalization. Error bars represent the standard deviation of a minimum of three CV curves collected from the same measurement with a 200 mV/s scan rate.

matrix may cause matrix effects, which may influence the signal intensities of other measured ions. The PDA deposition at the ITO interface therefore causes not only an increase of the CN$^-$ signal (arrows in Figure 4a,b) but also a slight decrease of the Si$^-$ signal and a slight increase of the InO$_2^-$ signal. The steep and sudden increase in the intensity of the InO$_2^-$ signal indicates the start of the ITO electrode. This change in the matrix causes fluctuations in the other (Si$^-$ and CN$^-$) signals, which are therefore excluded from interpretation. In summary,

the ToF-SIMS depth profiling shows that PDA is present in all coated samples at the ITO working electrode interface, as well as at the silica mesopore walls (Figure 4d). At the same time, an increase in the number of CV cycles during electropolymerization from 5 to 15 cycles causes a significant increase of the PDA deposition at type-A films.

By combining the findings from all methods mentioned above, we illustrated the distribution of PDA inside and outside of the nanopores of our silica films (Figure 4d). We

used red boxes to represent a certain area containing similar amounts of silica (light gray color) and changing amounts of PDA (dark gray colored film) in nanopores. Our characterizations imply that for type-A as well as for type-B films, PDA forms a film directly at the ITO surface and also forms particles in solution that deposit inside as well as on top of the membrane. The PDA deposition at all three sections (ITO surface, inside the pores, and membrane surface) increases with the number of CV cycles. This can already be concluded by the observed electrochemical current intensities and is further supported by our spectroscopic and microscopic measurements. To our knowledge, the more concentrated PDA at the surface of ITO (mesoporous film/ITO interface) should also impact the transport of anions and cations from the electrolyte toward the working electrode (ITO). Therefore, to (i) see the effect of PDA's presence at nanoconfinement on the ionic nanopore permselectivity as well as to (ii) reinforce our theory that a larger number of electropolymerization cycles increase the PDA deposition on the ITO surface, we studied the ionic nanopore transport of our mesoporous films before and after their functionalization with PDA (Figures 5 and 6).

Ionic Nanopore Transport at PDA-Functionalized Nanopores. pH-dependent ionic nanopore transport through mesoporous silica films is a promising technology for various applications such as sensing, desalination, and energy conversion.[10,59−62] Here, ionic nanopore transport at changing bulk pH was studied by cyclic voltammetry to understand the role of PDA presence and amount at the nanoporous and mesoporous film surface. Cyclic voltammetry measurements were performed when the PDA-functionalized mesoporous films were in contact with an aqueous electrolyte solution, containing anionic ($[Fe(CN)_6]^{3-/4-}$) (Figures 5 and 6a−c) or cationic ($[Ru(NH_3)_6]^{2+/3+}$) (Figures 5 and 6d−f) redox probes. The electrolyte solution pH is thereby adjusted to pH = 2 (red), pH = 5 (black), or pH = 8 (blue) (Figures 5 and 6a−f). From the oxidation peak of cyclic voltammograms (Figures 5a−f and 6a−f), we derived the anodic peak current density ($i_{p,a}$, Figure S12) quantifying the changes in the ionic nanopore accessibility (Figures 5g−h and 6g−h). These changes in the nanopore accessibility for different type-A and type-B films are illustrated in the insets of Figures 5 and 6a−f.

For nonfunctionalized type-A films at acidic pH, a larger number of anionic probes ($[Fe(CN)_6]^{3-/4-}$) access the mesoporous film, which is reflected in a higher value for the peak current density ($i_{p,a}$) at acidic conditions as compared to the basic electrolyte solution pH (Figure 5a,g). As expected, this pH dependence is reversed for the cationic probe ($[Ru(NH_3)_6]^{2+/3+}$, Figure 5d,h), which is ascribed to deprotonation of the silica surface (negatively charged silanol groups, Si−O$^-$, inset in Figure 5g). A similar pH influence was observed for the mesopore accessibility of both anionic (Figure 5b,c) and cationic (Figure 5e,f) redox probes through PDA-functionalized type-A silica mesopores. Moreover, as shown in Figure 5g,h, the increasing amount of PDA at higher electropolymerization cycles gradually limits the overall mesopore accessibility of both anions and cations, which is reflected in decreasing $i_{p,a}$ with increasing the PDA electropolymerization cycle number. As known from the literature[39−41] and confirmed by our reference experiments on planar ITO surfaces (Figure S15), PDA-film-coating on a conductive surface (e.g., gold, ITO) can regulate the ionic electrode accessibility through itself, thanks to (i) film thickness related spatial blocking and (ii) due to its

zwitterionic nature that can protonate at low pH and deprotonate at high pH (inset Figure 5g). However, ionic transport results from our plain PDA film coated on planar ITO reveals that, regardless of the changing PDA amount (at 5 or 15 electropolymerization cycles) and pH-dependent PDA charging, the presence of the plain PDA film almost fully blocks the transport of anions and cations (Figure S13c,d). Also, CV data collected during electropolymerization in Figure 2 show that the plain PDA-coating directly on ITO is more efficient (Figure 2a) than PDA-functionalized mesoporous films on top of ITO (Figure 2b,c). This demonstrates that in the presence of a larger surface area mesopore film on top of ITO, the electropolymerized PDA could find larger area to be localized and thus does not fully block—but limit—the access of ions through the functional nanopores. Therefore, in our PDA-functionalized type-A films, increasing the amount of PDA (at the mesoporous film/ITO interface) with 15 electropolymerization cycles results in blocking for ion transport (Figure 5g,h). In the absence of nanopore (de)-protonation at acidic pH 2 (Figure 5g,h), there is significant pore blocking of both anions and cations at higher PDA-deposited films. However, inside both 5 (Figure 5e) and 15-cycle (Figure 5f) functionalized silica mesopores, at basic solution pH, deprotonation of silica walls and PDA (inset Figure 5g) seems to result in overcoming this ion exclusion and the cations are electrostatically attracted, which is reflected in increasing $i_{p,a}$ for $[Ru(NH_3)_6]^{2+/3+}$. Although the overall peak current density is reduced for both ions with increasing PDA amounts, indicating less mesopore accessibility, we could still detect electrostatic attraction of deprotonated walls (and PDA) for cations at basic pH (Figure 5h). This possibility of cations accessing the highly PDA-loaded mesopores agrees with the previous literature of our group.[63−65]

Gradual limit of ionic nanopore transport while keeping the correlation between ionic transport and solution pH identical (as for pristine silica mesopores) is a versatile tool to extend the ionic permselectivity performance of the mesoporous films. For instance, anion transport between pH = 2 and 8 at nonfunctional silica nanopores is limited between peak current densities of ca. 140 and 100 μA/cm^2 (Figure 5g). Only by increasing the PDA deposition, we gradually hindered the anion transport, detected lower $i_{p,a}$ at the pores at all pH levels. To understand the existence of the PDA layer on the mesoporous silica surface and its role on the ionic nanopore transport, we partially removed the PDA from the surface of 15 cycles of PDA-functionalized type-A film by using CO_2-plasma cleaning (Figure S14). After CO_2 cleaning, higher anionic probe acceptance to the nanopores was detected at all pH levels compared to those before CO_2-plasma cleaning (Figure S14b). However, the $i_{p,a}$ from the CO_2-plasma cleaned films are still smaller than those from pristine and 5-cycle PDA electropolymerized type-A mesoporous silica films. This indicates that the surface PDA groups exist and play a role in the ionic transport, but still, the main ionic transport limiting effect is the PDA at the film/ITO interface.

The effect of PDA functionalization on ionic nanopore transport was also confirmed for the type-B films at different pH conditions (Figure 6) and illustrated in the insets of Figure 6a−f. Similar to type-A films, also the nonfunctionalized type-B films, at acidic pH (pH 2), show accessibility to the nanopores for cationic and anionic probe molecules since no electrostatic forces are acting between pore walls and the ionic probes (Figure 6a,d). Upon increasing the pH, the nonfunctionalized

pores are negatively charged and electrostatically exclude anions while attracting and preconcentrating the cations (Figure 6g–h). At acidic conditions (pH = 2), when the type-B film nanopores were loaded with larger PDA, unlike the type-A films, we did not observe a significant change in the cationic transport. Only a slight limit of anion mesopore accessibility was detected when the pores were loaded with PDA after 15 electropolymerization cycles (Figure 6c,f–h). As shown previously in Figure 5, 15 cycles of PDA functionalization at the type-A films could effectively limit the transport of both anions and cations. However, for type-B films, even at the largest number of (15 cycles) PDA present at the nanopores does not effectively block the ionic mesopores accessibility, which indicates a more complex influence of the mesopore structure on PDA electropolymerization and resulting ionic pore accessibility.

In the CV curves presenting the cationic ($[Ru(NH_3)_6]^{2+/3+}$) ion transport at type-A (Figure 5d–f) and type-B films (Figure 6d–f), with higher bulk pH, we detected broadening of the anodic and cathodic peaks and a reduction peak shift to lower potentials. In good agreement with the previous literature, such peak broadening is simply the result of increasing cationic probe and deprotonated pore wall interaction at higher pH conditions.[66−69] Also, the observed peak shift at higher pH conditions in the CV curves from cationic probe measurements can be attributed to the effect of the acid–base equilibrium on the Donnan potential of the films and electrolytes in contact.[66,70] At the same time, compared to the ionic pore accessibility at type-A films, at pH 5 and 8, in type-B films, when the pores were functionalized by 5 cycles of PDA, the PDA-functionalized pores contained a slightly higher concentration of anions and lower concentration of cations at the 5-cycle functionalized pores as compared to the non-functionalized deprotonated pores (Figure 6b,e,g,h). This is probably related to the presence of PDA (even if it is also deprotonated), which to some extent limits (isolates) the electrostatic effect of the deprotonated silica walls ($Si-O^-$) acting on attracting the anions and rejecting the cations. Finally, at the highest amount of PDA-deposited silica mesopores and at high pH conditions, the type-B pores could reject almost entirely the transport of anions due to pore blocking (by PDA) and electrostatic rejection between the probes and the deprotonated pore walls (silica and PDA) (Figure 6c,g). However, similar to the type-A films, deprotonated silica and PDA at type-B nanopores at high pH could help the cationic probe access the nanopores via electrostatic attraction (Figure 6h).

As shown previously for type-A films, the solution-pH-related ionic transport mechanism of type-B films does not change upon PDA functionalization. Additionally, except for the 5 cycles of PDA-functionalized type-B films where slight enhancement of anion mesopore accessibility happens at different solution pH values, similar to type-A films, we observed more limited ionic transport via larger PDA deposition at type-B films too (Figure 6g,h). Toward applying PDA electropolymerization for different nanopore functionalization, it is important to note that the effect of PDA is not limited exclusively toward hindering the ionic transport; it can also advance the pH-related ionic nanopore transport.

CONCLUSIONS

We demonstrate silica mesoporous film functionalization using the electropolymerization of polydopamine (PDA) inside two structurally different mesoporous silica films. For both mesoporous films coated on top of the ITO working electrode, PDA deposits upon polymerization directly at the ITO/film interface as well as on the inner surface of the pores and on top of the membrane. An increase in the number of electropolymerization cycles causes an increase of the PDA formation and subsequent deposition in all sections of the films. The total amount of PDA formation per ITO surface area does not significantly differ between the two samples. The presence of PDA in type-A and type-B nanopores influences pH-dependent ionic nanopore accessibility. We detected pH-dependent ionic transport only through mesoporous films carrying PDA but not through plain PDA films deposited directly on the working electrode. For both PDA-functionalized type-A and type-B mesoporous silica films, ionic nanopore transport is regulated by (1) the PDA amount and its distribution at nanopores, (2) the deprotonation of silica pore walls and PDA at high pH, and (3) the electrolyte (bulk) pH. Here, we introduced electropolymerization as a new tool to precisely functionalize mesoporous films while being able to tune the polymer amount and its distribution in the film. We envision that this new method will not only be employed for the regulation of ionic transport in nanopores but also provide a versatile platform for the precise functionalization of porous materials.

EXPERIMENTAL SECTION

Chemicals. Tetraethyl orthosilicate (TEOS) (98% reagent grade), Pluronic F127 (BioReagent grade), ethanol (absolute EMPLURA), hydrochloric acid (37%), potassium hexacyanoferrate(III) (99.95%), sodium phosphate dibasic anhydrous (99%), sodium phosphate monobasic (99%), and dopamine hydrochloride were purchased from Sigma-Aldrich/Merck. Potassium chloride (99.5%) was purchased from Carl Roth. Hexaammineruthenium(II) chloride (99.9%) was purchased from Alfa Aesar.

Mesoporous Silica Thin-Film Fabrication. Mesoporous silica thin films were prepared through sol–gel chemistry using tetraethyl orthosilicate (TEOS) as an inorganic precursor and the amphiphilic triblock copolymer Pluronic F127 as a structure-directing template that undergoes micellization upon solvent evaporation. According to reported protocols,[49] the molar ratios of the sol–gel precursor solutions were set to (1) 1 TEOS:0.0075 F127:40 ethanol:10 water:0.28 HCl and (2) 1 TEOS:0.009 F127:19 ethanol:14 water:0.015 HCl leading to (1) type-A and (2) type-B mesoporous films. The sol–gel precursors were prepared at room temperature, with the first suspension of Pluronic F127 in ethanol under stirring. Upon adding a freshly prepared hydrochloric acid solution (37%) in water (1:1.55; 2:0.05 mol/L), the template dissolved immediately. After the addition of TEOS, the solution was stirred overnight at room temperature and stored at −18 °C. Prior to dip-coating, the sol–gel solutions were stirred for 30 min at room temperature, and the substrates (ITO-coated glass (Delta Technologies, 70−100 Ω) and silicon wafer (Si-Mat)) were cleaned with ethanol-soaked fabrics. Then, the substrates were dip-coated at a withdrawal speed of 2 mm/s under controlled environmental conditions (50% relative humidity, 22−25 °C) using the previously reported evaporation-induced self-assembly (EISA) process.[71] After aging under the controlled climate conditions for 60 min, the films were subjected to the following temperature treatment: heating up to 60 °C within 10 min and holding the temperature for 60 min, followed by a temperature increase to 130 °C within 10 min and holding the temperature for 60 min. Subsequently, the temperature was increased to 350 °C with a heating rate of 1 °C/min, with the final temperature maintained for 2 h.

Electropolymerization and Electrochemical Analysis. Polydopamine electropolymerization was performed via cyclic voltammetry with a standard three-electrode configuration and a Metrohm

Autolab N series potentiostat (AU-TOLAB PGSTAT 204). Plain ITO and ITO covered with mesoporous membranes (type-A and type-B) were used as working electrodes, and Ag/AgCl (3 M KCl) was used as the reference electrode. The experiments were performed in an environmental atmosphere at room temperature. For the film deposition, a 1 mg/mL dopamine solution in 100 mM phosphate buffer (PB, pH = 7.0) was used. The PB was prepared with sodium phosphate dibasic anhydrous and sodium phosphate monobasic and Milli-Q water and was purged with nitrogen for at least 15 min for all experiments to remove the dissolved oxygen and prevent dopamine self-polymerization. The working electrodes were either not pretreated (ToF-SIMS measurement of type-A 15c and type-B 5c) or immersed in PB that was constantly purged with nitrogen for 15 min to ensure no oxygen is trapped in the membrane pores (all other samples). ToF-SIMS surface maps (Figure S11) of a blank type-A sample (for reference) and nonpretreated 15c type-A and 5c type-B samples show an increase of CN^- signals that overshadow SiO_2^- signals for the two coated samples, indicating a strong surface deposition of PDA. In order to inhibit and control the surface deposition, we introduced the incubation of the samples in nitrogen-purged PB. The pretreatment was conducted to inhibit growth of PDA on top of the membrane, but it is expected to not significantly change the polymerization conditions inside the nanopores. Depositions via CV were performed in a potential range of −500 to +500 mV vs Ag/AgCl at a scan rate of 10 mV/s for either 5 or 15 cycles. Fifteen post-CV cycles were performed under the same conditions, but in a monomer-free PB. The coated working electrodes were stored under an argon atmosphere. Two different CV setups were used: analytical electrochemical measurements and the respective synthesis were conducted in a horizontal cell setup that allows to define a surface area during synthesis and analysis (Figure S15a). Before and after the film deposition, analytical cyclovoltammetry (15 cycles, 10 mV/s) in the potential window from −750 to +750 mV was conducted. This wider window is necessary to detect the peaks that indicate the formation of polydopamine. A gold wire was used as the counter electrode in this setup. Cyclovoltammetric analysis (from −1 to 1 V) of the oxidation and reduction of 1 mM potassium ferrocyanide in 100 mM nitrogen-purged PB was conducted in the horizontal cell (Figure S3) with a scan rate of 100 mV/s. The cyclovoltammetric analysis of oxygen reduction on plain ITO in nonpurged PB and in nitrogen-purged PB was conducted in a potential window from −0.8 to 0.8 V at a scan rate of 10 mV/s with 100 mM phosphate buffer at pH 7 (Figure S5). The synthesis of samples for all other analytical measurements was conducted in a vertical cell setup (Figure S15b). This setup allows for electropolymerization on larger surface areas, which is necessary for subsequent ionic permeability studies. A platinum-coated titanium mesh was used as the counter electrode in this setup. Figure S7 shows the synthesis (a) and post-cross-linking (b) of all sample types (plane ITO, sample type-A and sample type-B) over 15 CV cycles. The decrease in current during the cross-linking procedure throughout the progression of the CV cycles indicates the oxidation of PDA, which causes cross-linking. The limited change in the last cycles indicates that most PDA got cross-linked.[32] The "current density" describes the current per surface area of our samples, not the current per free electrode area.

Transmission Electron Microscopy (TEM) Imaging. Transmission electron micrographs were collected using a Philips FEI CM-20 transmission electron microscope (Philips, Amsterdam, the Netherlands) operating at an accelerating voltage of 200 kV. Samples for TEM imaging were prepared by scratching the mesoporous films and subsequently dispersing the scratched film in absolute ethanol during 5 min of sonication. After ultrasonication, mesoporous film-loaded ethanol suspension was drop-cast onto 3.05 mm Cu grids (mesh size 200) with a Lacey carbon film on the top (Plano GmbH, Wetzlar, Germany), placed on the top of a filter paper. After the drop-cast, samples were left for drying under ambient conditions.

Attenuated Total Reflection Fourier Transform Infrared (ATR-FTIR) Spectroscopy. IR spectra were recorded in attenuated total reflection (ATR) mode using a Spectrum One Fourier transformation infrared (FTIR) spectrometer from PerkinElmer at 4000−650 cm^{-1}. For the measurements performed with 32 scans per sample, the films were either scratched off the substrate using a razor blade, placed on top of the ATR-IR crystal, or left on the substrate and pressed onto the ATR crystal with constant contact pressure. The resulting spectra were background-corrected using the device software's background correction tool and normalized to the Si−O−Si asymmetric stretching vibrational band at approximately 1060 cm^{-1} by using IgorPro 7.08 (WaveMetrics). To quantify the relative change of PDA amount at mesoporous films, the normalized ν_{ring} (C=C) stretching mode and N−H bending mode vibration peak intensities ($I(1650$ cm$^{-1})/I(1060$ cm^{-1})) from PDA-functionalized films data were divided to $I(1650$ cm$^{-1})/I(1060$ cm^{-1}) calculated from the mesoporous films before their PDA functionalization (see Figure S8e for bar graphs before the final normalization).

Ellipsometry. Ellipsometry was employed for the determination of refractive indices and thicknesses of mesoporous silica thin films deposited on silicon wafer substrates (Si-Mat, Kaufering, Germany, 100 mm diameter, 525 ± 25 μm thickness, type P/Bor, ⟨100⟩ orientation, CZ growth method, 2−5 W resistivity, polished on one side) using the nanofilm EP3-SE device (Accurion) equipped with a 658 nm laser. The software EP4-View and EP4-model (version 1.2.0) were used for measurements and model analysis. The angle of incidence (AOI) was varied from 38 to 68° in 2° increments and measured in one-zone mode (Si-wafer → SiO_2 oxide layer → SiO_2 mesoporous layer). The measurements were performed under controlled humidity conditions (15% relative humidity) adjusted by the ACEflow 1.0 (SOLGELWAY) system and regulated by Regul'Hum (version 3.3) software. The average pore volume calculation was done by using the refractive indices according to Brüggemann's effective medium theory described in the literature.[72]

Static Contact Angle (CA$_{static}$) Measurements. Contact angles (CA$_{static}$) were measured as deposited with an OCA 35 device by DataPhysics using the SCA 4.5.2 software and the sessile drop method under a standard atmosphere (T = 23 °C, RH = 60%). A drop volume of 2 μL was used, and the CA$_{static}$ value was obtained by fitting the droplet shape by using the approximation algorithm of the SCA software. The mean CA$_{static}$ was measured for at least five droplets. CA$_{static}$ measurements of regions previously investigated for ionic nanopore transport (see Figure S8a) were very limited (0.21 cm^2 circular) for leaving five different droplets. Therefore, we could generate only one CA$_{static}$ from these measurements; thus, no standard deviations (error bars) could be generated.

Krypton Physisorption. Pore and pore neck sizes of type-A and type-B films were obtained by Krypton physisorption measurements at 87.4 K using an Autosorb iQ instrument (Anton Paar, Ostfildern-Scharnhausen, Germany). The temperature of 87.4 K was adjusted by using (i) liquid argon and a saturation pressure of 12 Torr or (ii) a cryo sync (Anton Paar, Ostfildern-Scharnhausen, Germany) and a saturation pressure of 12.9 Torr. Before each measurement, the samples were degassed at 80 °C for 12 h under a high vacuum. The adsorption isotherms were evaluated with respect to the pore size and pore size distribution by using the Krypton 87.4 K thin-film method, which is implemented in the ASiQwin program (Anton Paar, Ostfildern-Scharnhausen, Germany). The Barrett−Joyner−Halenda (BJH) method was applied to the desorption branch of the isotherms to calculate the pore neck size.

Scanning Force Microscopy (SFM). Scanning force microscopy (SFM) was performed in peak force mode in the dry state on a BRUKER Dimension ICON. We used an Al-coated OLTESPA cantilever from OPUS by MikroMasch (nominal resonance frequency 70 kHz, nominal spring constant 2 N/m). For imaging, we used 512 × 512 pixels for all scan sizes of 1 μm^2. The roughness values S_Q of a whole map as well as of inside 200 nm × 200 nm areas (marked with white borders in the images) are collected for three spots on each sample type, and their averages and standard deviations are calculated. In addition to topography, we recorded adhesion maps with identical settings. The data was processed by the software Gwyddion (v2.62). Topography images were leveled by the mean plane subtraction and

the mean and matching row alignment function. The adhesion data was not postprocessed.

Time-of-Flight Secondary Ion Mass Spectrometry (ToF-SIMS) and Quantification of the PDA Amount at Mesoporous Films. ToF-SIMS depth profiles were acquired in the negative ion polarity using a TOF.SIMS5.NCS (IONTOF, Münster, Germany) with 30 keV Bi^{3+} primary ions (current 0.13 pA) for analysis and 10 keV Ar1500 ions for sputtering at a current of 10.5 nA the noninterlaced sputtering mode. The primary ion gun analyzed a 200 × 200 μm^2 field of view with a 128 pixels × 128 pixels raster. The sputter erosion was conducted on an area of 400 μm × 400 μm^2. The analyzer cycle time was 200 μs, relating to a mass range of 1−3600 m/z. Data evaluation of the data sets was done with the IONTOF Surface Lab 7.1 evaluation software. The graphs for the plain samples (Figure 4a,b) were smoothened via the averaging of two adjacent data points.

Ionic Transport Experiments by Cyclic Voltammetry and Peak Current Density Quantification. Cyclic voltammetry measurements were performed by using an Autolab PGSTAT302N potentiostat from Metrohm Autolab BV operated by Nova 2.0 software called Nova 2.0. The pore transport was analyzed by using electrolytes consisting of 100 mmol/L KCl and 1 mmol/L $[Fe(CN)_6]^{3-/4-}$, or 1 mmol/L $[Ru(NH_3)_6]^{2+/3+}$ as negatively or positively charged probe molecules. The pH values of the electrolyte solutions were adjusted to pH 3, 5, and 8 using an Edge pH meter (Hanna Industries) and diluted aqueous hydrochloric acid and sodium hydroxide solutions. For cyclic voltammetry measurements, a three-electrode system consisting of an Ag/AgCl electrode (BASi, Type RE-6) as the reference electrode, a graphite electrode (Alfa Aesar) as the counter electrode, and the ITO layer of the silica-coated substrate (Delta Technologies, 70−100 Ω) as the working electrode was used. For the anionic redox probe $[Fe(CN)_6]^{3-/4-}$, the potential range was set to −0.2 to 0.6 V, while for the cationic probe $[Ru(NH_3)_6]^{2+/3+}$, it was set to −0.6 to 0.2 V. Before each cyclic voltammetry measurement, the samples were incubated in 100 mmol/L KCl solution for at least 1 h. The contact area (opening) between the electrolyte and the measured mesoporous film was 0.21 cm^2. Each condition was measured at least once, using a scan rate sequence of 200, 100, 25, 300, 500, and 200 mV/s, while each scan rate cycled three times. For evaluation, the 200 mV/s scan rate was used only if 200 mV/s CV curves collected at the beginning and end agreed with each other. Measurements of one series were repeated, until a constant current density in relation to the electrolyte exposure time was reached. Anodic peak current densities ($i_{p,a}$) were quantified from the peaks in the oxidation part after defining a proper baseline correction as explained in the literature.[12,73] A previous study by Alberti et al. showed that similar mesoporous films might get damaged after a critical time and continuous electrochemical investigations, which could influence the collected data.[74] To avoid such risks in our measurement, while studying the nanopore transport of a film, we changed the measurement position (where the film was in contact with the electrolyte at the 0.21 cm^2 opening) every time the electrolyte was changed (having a different pH and/or ionic probe). Also, the contact time of films with electrolytes was less than 1.30 h to avoid possible deformations at the film surface under electrochemical conditions. Therefore, we avoided collecting data from already studied regions and kept the interaction time between the electrolyte and the (non-)functional films as short as possible.

ASSOCIATED CONTENT

Supporting Information

The Supporting Information is available free of charge at https://pubs.acs.org/doi/10.1021/acs.chemmater.3c01890.

> Detailed description of the CO_2-plasma cleaning, transmission electron microscopy image analysis, and electrochemical differential pulse voltammetry (DPV) measurement methods; graph showing the pore size distribution results ($dV(d)$ versus pore diameter) of

type-A and type-B films; TEM micrographs of both type-A and type-B films before and after their image analysis by using thresholding routine in ImageJ and the histograms of the pore neck opening obtained from these image analyses; cyclovoltammetric analysis of the oxidation and reduction of 1 mM potassium ferrocyanide on plain ITO, type-A, and type-B film; analytical CV plots collected from a constant electrode surface area in the horizontal cell setup before and after the PDA functionalization of plain ITO, type-A, and type-B samples; cyclovoltammetric analysis of plain ITO in nonpurged PB and in nitrogen-purged PB; DPV plots of plain ITO and type-A film-coated ITO before and after PDA functionalization; CV curves collected during and after 15-cycle electropolymerization on plain ITO, type-A, and type-B films in the vertical cell setup where the polymerization area was not limited; static contact angle (CA_{static}) data of PDA-(non)functionalized mesoporous films and plain ITO together with CA_{static} recorded from the area where the ionic nanopore transport was studied from the 5-cycle PDA-functionalized type-A and type-B films; ATR-IR spectra of the PDA-functionalized plain ITO (no mesoporous film on the top), type-A, and type-B films with different functionalization cycles; height and adhesion maps collected from the SFM measurements of the mesoporous film samples with and without PDA functionalization; lateral SiO_2^- and CN^- ToF-SIMS intensity maps of mesoporous films before and after their PDA functionalization; CV curves collected while studying the nanopore accessibility of anionic and cationic redox probes though nonfunctionalized type-A films at different pH and they show how anodic peak current density ($i_{p,a}$) was quantified; CV curves and calculated $i_{p,a}$ presenting the ionic transport through plain PDA deposited on ITO (no mesoporous films) together with the transport through (non)-PDA-functionalized mesoporous films; CV curves and $i_{p,a}$ calculated from these curves presenting the changes in the ionic nanopore accessibility of 15-cycle functionalized type-A films after its CO_2-plasma cleaning; and horizontal and vertical setups used for PDA functionalization (PDF)

AUTHOR INFORMATION

Corresponding Authors

H. Samet Varol − Ernst-Berl Institut für Technische und Makromolekulare Chemie, Technische Universität Darmstadt, 64287 Darmstadt, Germany; Department of Chemistry "Giacomo Ciamician", Università degli Studi di Bologna, 40126 Bologna, Italy; orcid.org/0000-0001-8245-2243; Email: samet.varol@unibo.it

Annette Andrieu-Brunsen − Ernst-Berl Institut für Technische und Makromolekulare Chemie, Technische Universität Darmstadt, 64287 Darmstadt, Germany; orcid.org/0000-0002-3850-3047; Email: annette.andrieu-brunsen@tu-darmstadt.de

Authors

Tilmann Herberger − Max Planck Institute for Polymer Research, 55128 Mainz, Germany

Marius Kirsch − Ernst-Berl Institut für Technische und Makromolekulare Chemie, Technische Universität Darmstadt, 64287 Darmstadt, Germany

Joanna Mikolei − *Ernst-Berl Institut für Technische und Makromolekulare Chemie, Technische Universität Darmstadt, 64287 Darmstadt, Germany*

Lothar Veith − *Max Planck Institute for Polymer Research, 55128 Mainz, Germany*

Venkataprasanna Kannan-Sampathkumar − *Max Planck Institute for Polymer Research, 55128 Mainz, Germany*

Raoul D. Brand − *Institute of Physical Chemistry, Justus-Liebig University, 35392 Giessen, Germany*

Christopher V. Synatschke − *Max Planck Institute for Polymer Research, 55128 Mainz, Germany*

Tanja Weil − *Max Planck Institute for Polymer Research, 55128 Mainz, Germany;* orcid.org/0000-0002-5906-7205

Author Contributions

[⊥]H.S.V. and T.H. are co-first authors.

Notes

The authors declare no competing financial interest.

■ REFERENCES

(1) Corry, B.; Chung, S. H. Mechanisms of Valence Selectivity in Biological Ion Channels. *Cell. Mol. Life Sci.* 2006, 63 (3), 301−315.

(2) Patel, S. S.; Belmont, B. J.; Sante, J. M.; Rexach, M. F. Natively Unfolded Nucleoporins Gate Protein Diffusion across the Nuclear Pore Complex. *Cell* 2007, 129 (1), 83−96.

(3) Epsztein, R.; Duchanois, R. M.; Ritt, C. L.; Noy, A.; Elimelech, M. Towards Single-Species Selectivity of Membranes with Subnanometre Pores. *Nat. Nanotechnol.* 2020, 15, 426−436.

(4) Gourmand, C.; Bertagnolli, C.; Brandel, J.; Hubscher-Bruder, V.; Boos, A. Bioinspired Mesoporous Silica for Cd(II) Removal from Aqueous Solutions. *Ind. Eng. Chem. Res.* 2022, 61 (23), 8188−8203.

(5) Bandehali, S.; Parvizian, F.; Hosseini, S. M.; Matsuura, T.; Drioli, E.; Shen, J.; Moghadassi, A.; Adeleye, A. S. Planning of Smart Gating Membranes for Water Treatment. *Chemosphere* 2021, 283, No. 131207.

(6) Sanchez, C.; Belleville, P.; Popall, M.; Nicole, L. Applications of Advanced Hybrid Organic−Inorganic Nanomaterials: From Laboratory to Market. *Chem. Soc. Rev.* 2011, 40 (2), 696−753.

(7) Sui, S.; Zhang, H.; Du, S. *Nanoporous Materials for Molecule Separation and Conversion*; Elsevier, 2020, pp 441−476.

(8) Yaroshchuk, A. Evaporation-Driven Electrokinetic Energy Conversion: Critical Review, Parametric Analysis and Perspectives. *Adv. Colloid Interface Sci.* 2022, 305, No. 102708.

(9) Soozanipour, A.; Sohrabi, H.; Abazar, F.; Khataee, A.; Noorbakhsh, A.; Asadnia, M.; Taheri-Kafrani, A.; Majidi, M. R.; Razmjou, A. Ion Selective Nanochannels: From Critical Principles to Sensing and Biosensing Applications. *Adv. Mater. Technol.* 2021, 6 (10), No. 2000765.

(10) Ito, T.; Nathani, A. Electrochemical Sensing at Nanoporous Film-Coated Electrodes. *Electrochem. Sci. Adv.* 2022, 2 (5), No. e2100126.

(11) Pardehkhorram, R.; Andrieu-Brunsen, A. Pushing the Limits of Nanopore Transport Performance by Polymer Functionalization. *Chem. Commun.* 2022, 58 (34), 5188−5204.

(12) Varol, H. S.; Förster, C.; Andrieu-Brunsen, A. Ligand-Binding Mediated Gradual Ionic Transport in Nanopores. *Adv. Mater. Interfaces* 2023, 10, No. 2201902.

(13) Schoch, R. B.; Han, J.; Renaud, P. Transport Phenomena in Nanofluidics. *Rev. Mod. Phys.* 2008, 80 (3), 839−883.

(14) Silies, L.; Didzoleit, H.; Hess, C.; Stühn, B.; Andrieu-Brunsen, A. Mesoporous Thin Films, Zwitterionic Monomers, and Iniferter-Initiated Polymerization: Polymerization in a Confined Space. *Chem. Mater.* 2015, 27 (6), 1971−1981.

(15) Silies, L.; Andrieu-Brunsen, A. Programming Ionic Pore Accessibility in Zwitterionic Polymer Modified Nanopores. *Langmuir* 2018, 34 (3), 807−816.

(16) Boysen, R. I.; Schwarz, L. J.; Nicolau, D. V.; Hearn, M. T. W. Molecularly Imprinted Polymer Membranes and Thin Films for the Separation and Sensing of Biomacromolecules. *J. Sep. Sci.* 2017, 40 (1), 314−335.

(17) Kausar, A. Polymer Coating Technology for High Performance Applications: Fundamentals and Advances. *J. Macromol. Sci., Part A: Pure Appl. Chem.* 2018, 55 (5), 440−448.

(18) Alfieri, M. L.; Weil, T.; Ng, D. Y. W.; Ball, V. Polydopamine at Biological Interfaces. *Adv. Colloid Interface Sci.* 2022, 305, No. 102689.

(19) Stöckle, B.; Ng, D. Y. W.; Meier, C.; Paust, T.; Bischoff, F.; Diemant, T.; Behm, R. J.; Gottschalk, K. E.; Ziener, U.; Weil, T. Precise Control of Polydopamine Film Formation by Electropolymerization. *Macromol. Symp.* 2014, 346 (1), 73−81.

(20) Sharma, P. S.; Pietrzyk-Le, A.; D'Souza, F.; Kutner, W. Electrochemically Synthesized Polymers in Molecular Imprinting for Chemical Sensing. *Anal. Bioanal. Chem.* 2012, 402 (10), 3177−3204.

(21) Becker, E.; Parashkov, R.; Ginev, G.; Schneider, D.; Hartmann, S.; Brunetti, F.; Dobbertin, T.; Metzdorf, D.; Riedl, T.; Johannes, H. H.; Kowalsky, W. All-Organic Thin-Film Transistors Patterned by Means of Selective Electropolymerization. *Appl. Phys. Lett.* 2003, 83 (19), 4044−4046.

(22) Salinas, G.; Arnaboldi, S.; Bouffier, L.; Kuhn, A. Recent Advances in Bipolar Electrochemistry with Conducting Polymers. *ChemElectroChem* 2022, 9 (1), No. e202101234.

(23) Plamper, F. A. Polymerizations under Electrochemical Control. *Colloid Polym. Sci.* 2014, 292 (4), 777−783.

(24) Mattarozzi, M.; Giannetto, M.; Secchi, A.; Bianchi, F. Novel Coating for Solid-Phase Microextraction: Electropolymerization of a Molecular Receptor Functionalized with 2,2′-Bithiophene for the Determination of Environmental Pollutants at Trace Levels. *J. Chromatogr. A* 2009, 1216 (18), 3725−3730.

(25) Kund, J.; Daboss, S.; D'Alvise, T. M.; Harvey, S.; Synatschke, C. V.; Weil, T.; Kranz, C. Physicochemical and Electrochemical

Characterization of Electropolymerized Polydopamine Films: Influence of the Deposition Process. *Nanomaterials* **2021**, *11* (8), No. 1964.

(26) Schopf, G.; Koßmehl, G. Advances in Polymer Science; *Polythiophenes—Electrically Conductive Polymers*, Springer: Berlin, Heidelberg, 1997; p 129. DOI: 10.1007/BFb0111619.

(27) Ullah, W.; Herzog, G.; Vilà, N.; Walcarius, A. Polyaniline Nanowire Arrays Generated through Oriented Mesoporous Silica Films: Effect of Pore Size and Spectroelectrochemical Response. *Faraday Discuss.* **2022**, *233*, 77−99.

(28) Plamper, F. A. Changing Polymer Solvation by Electrochemical Means: Basics and Applications. *Adv. Polym. Sci.* **2015**, *266*, 125−212.

(29) Malollari, K. G.; Delparastan, P.; Sobek, C.; Vachhani, S. J.; Fink, T. D.; Zha, R. H.; Messersmith, P. B. Mechanical Enhancement of Bioinspired Polydopamine Nanocoatings. *ACS Appl. Mater. Interfaces* **2019**, *11* (46), 43599−43607.

(30) Lynge, M. E.; Van Der Westen, R.; Postma, A.; Städler, B. Polydopamine—a Nature-Inspired Polymer Coating for Biomedical Science. *Nanoscale* **2011**, *3* (12), 4916−4928.

(31) Boecker, M.; Micheel, M.; Mengele, A. K.; Neumann, C.; Herberger, T.; Marchesi D'Alvise, T.; Liu, B.; Undisz, A.; Rau, S.; Turchanin, A.; Synatschke, C. V.; Wächtler, M.; Weil, T. Rhodium-Complex-Functionalized and Polydopamine-Coated CdSe@CdS Nanorods for Photocatalytic NAD+ Reduction. *ACS Appl. Nano Mater.* **2021**, *4* (12), 12913−12919.

(32) Marchesi D'Alvise, T.; Harvey, S.; Hueske, L.; Szelwicka, J.; Veith, L.; Knowles, T. P. J.; Kubiczek, D.; Flaig, C.; Port, F.; Gottschalk, K. E.; Rosenau, F.; Graczykowski, B.; Fytas, G.; Ruggeri, F. S.; Wunderlich, K.; Weil, T. Ultrathin Polydopamine Films with Phospholipid Nanodiscs Containing a Glycophorin A Domain. *Adv. Funct Mater.* **2020**, *30* (21), No. 2000378.

(33) Sensi, M.; Migatti, G.; Beni, V.; Marchesi D'alvise, T.; Weil, T.; Berto, M.; Greco, P.; Imbriano, C.; Biscarini, F.; Bortolotti, C. A. Monitoring DNA Hybridization with Organic Electrochemical Transistors Functionalized with Polydopamine. *Macromol. Mater. Eng.* **2022**, *307* (5), No. 2100880.

(34) Zhou, J.; Wang, P.; Wang, C.; Goh, Y. T.; Fang, Z.; Messersmith, P. B.; Duan, H. Versatile Core-Shell Nanoparticle@ Metal-Organic Framework Nanohybrids: Exploiting Mussel-Inspired Polydopamine for Tailored Structural Integration. *ACS Nano* **2015**, *9* (7), 6951−6960.

(35) Grześkowiak, B. F.; Maziukiewicz, D.; Kozłowska, A.; Kertmen, A.; Coy, E.; Mrówczyński, R. Polyamidoamine Dendrimers Decorated Multifunctional Polydopamine Nanoparticles for Targeted Chemo- and Photothermal Therapy of Liver Cancer Model. *Int. J. Mol. Sci.* **2021**, *22* (2), No. 738.

(36) Almeida, L. C.; Correia, R. D.; Marta, A.; Squillaci, G.; Morana, A.; La Cara, F.; Correia, J. P.; Viana, A. S. Electrosynthesis of Polydopamine Films - Tailored Matrices for Laccase-Based Biosensors. *Appl. Surf. Sci.* **2019**, *480*, 979−989.

(37) Jiang, Y.; Lan, Y.; Yin, X.; Yang, H.; Cui, J.; Zhu, T.; Li, G. Polydopamine-Based Photonic Crystal Structures. *J. Mater. Chem. C* **2013**, *1* (38), 6136−6144.

(38) Vasileiadis, T.; Marchesi D'Alvise, T.; Saak, C. M.; Pochylski, M.; Harvey, S.; Synatschke, C. V.; Gapinski, J.; Fytas, G.; Backus, E. H. G.; Weil, T.; Graczykowski, B. Fast Light-Driven Motion of Polydopamine Nanomembranes. *Nano Lett.* **2022**, *22* (2), 578−585.

(39) Yu, B.; Liu, J.; Liu, S.; Zhou, F. Pdop Layer Exhibiting Zwitterionicity: A Simple Electrochemical Interface for Governing Ion Permeability. *Chem. Commun.* **2010**, *46* (32), 5900−5902.

(40) Liu, Q.; Yu, B.; Ye, W.; Zhou, F. Highly Selective Uptake and Release of Charged Molecules by PH-Responsive Polydopamine Microcapsules. *Macromol. Biosci.* **2011**, *11* (9), 1227−1234.

(41) Gao, B.; Su, L.; Tong, Y.; Guan, M.; Zhang, X. Ion Permeability of Polydopamine Films Revealed Using a Prussian Blue-Based Electrochemical Method. *J. Phys. Chem. B* **2014**, *118*, 12781−12787.

(42) Pérez-Mitta, G.; Tuninetti, J. S.; Knoll, W.; Trautmann, C.; Toimil-Molares, M. E.; Azzaroni, O. Polydopamine Meets Solid-State Nanopores: A Bioinspired Integrative Surface Chemistry Approach to Tailor the Functional Properties of Nanofluidic Diodes. *J. Am. Chem. Soc.* **2015**, *137* (18), 6011−6017.

(43) Hu, S.; Yang, Z.; Wang, S.; Wang, L.; He, Q.; Tang, H.; Ji, P.; Chen, T. Zwitterionic Polydopamine Modified Nanoparticles as an Efficient Nanoplatform to Overcome Both the Mucus and Epithelial Barriers. *Chem. Eng. J.* **2022**, *428*, No. 132107.

(44) Xie, X.; Tang, J.; Xing, Y.; Wang, Z.; Ding, T.; Zhang, J.; Cai, K. Intervention of Polydopamine Assembly and Adhesion on Nanoscale Interfaces: State-of-the-Art Designs and Biomedical Applications. *Adv. Healthcare Mater.* **2021**, *10* (9), No. 2002138.

(45) Zheng, X.; Zhang, J.; Wang, J.; Qi, X.; Rosenholm, J. M.; Cai, K. Polydopamine Coatings in Confined Nanopore Space: Toward Improved Retention and Release of Hydrophilic Cargo. *J. Phys. Chem. C* **2015**, *119* (43), 24512−24521.

(46) Barclay, T. G.; Hegab, H. M.; Clarke, S. R.; Ginic-Markovic, M. Versatile Surface Modification Using Polydopamine and Related Polycatecholamines: Chemistry, Structure, and Applications. *Adv. Mater. Interfaces* **2017**, *4* (19), No. 1601192.

(47) Dai, M.; Sun, L.; Chao, L.; Tan, Y.; Fu, Y.; Chen, C.; Xie, Q. Immobilization of Enzymes by Electrochemical and Chemical Oxidative Polymerization of L-DOPA to Fabricate Amperometric Biosensors and Biofuel Cells. *ACS Appl. Mater. Interfaces* **2015**, *7* (20), 10843−10852.

(48) Dunphy, D. R.; Sheth, P. H.; Garcia, F. L.; Brinker, C. J. Enlarged Pore Size in Mesoporous Silica Films Templated by Pluronic F127: Use of Poloxamer Mixtures and Increased Template/SiO2 Ratios in Materials Synthesized by Evaporation-Induced Self-Assembly. *Chem. Mater.* **2015**, *27* (1), 75−84.

(49) Brilmayer, R.; Kübelbeck, S.; Khalil, A.; Brodrecht, M.; Kunz, U.; Kleebe, H. J.; Buntkowsky, G.; Baier, G.; Andrieu-Brunsen, A. Influence of Nanoconfinement on the PKa of Polyelectrolyte Functionalized Silica Mesopores. *Adv. Mater. Interfaces* **2020**, *7* (7), No. 1901914.

(50) Dominguez, H.; Allen, M. P.; Evans, R. Monte Carlo Studies of the Freezing and Condensation Transitions of Confined Fluids. *Mol. Phys.* **1999**, *96* (2), 209−229.

(51) Thommes, M.; Kaneko, K.; Neimark, A. V.; Olivier, J. P.; Rodriguez-Reinoso, F.; Rouquerol, J.; Sing, K. S. W. Physisorption of Gases, with Special Reference to the Evaluation of Surface Area and Pore Size Distribution (IUPAC Technical Report). *Pure Appl. Chem.* **2015**, *87* (9−10), 1051−1069.

(52) Varol, H. S.; Srivastava, A.; Kumar, S.; Bonn, M.; Meng, F.; Parekh, S. H. Bridging Chains Mediate Nonlinear Mechanics of Polymer Nanocomposites under Cyclic Deformation. *Polymer* **2020**, *200*, No. 122529.

(53) Varol, H. S.; Meng, F.; Hosseinkhani, B.; Malm, C.; Bonn, D.; Bonn, M.; Zaccone, A.; Parekh, S. H. Nanoparticle Amount, and Not Size, Determines Chain Alignment and Nonlinear Hardening in Polymer Nanocomposites. *Proc. Natl. Acad. Sci. U.S.A.* **2017**, *114* (16), E3170−E3177.

(54) Varol, H. S.; Sánchez, M. A.; Lu, H.; Baio, J. E.; Malm, C.; Encinas, N.; Mermet-Guyennet, M. R. B.; Martzel, N.; Bonn, D.; Bonn, M.; Weidner, T.; Backus, E. H. G.; Parekh, S. H. Multiscale Effects of Interfacial Polymer Confinement in Silica Nanocomposites. *Macromolecules* **2015**, *48* (21), 7929−7937.

(55) Alfieri, M. L.; Micillo, R.; Panzella, L.; Crescenzi, O.; Oscurato, S. L.; Maddalena, P.; Napolitano, A.; Ball, V.; D'Ischia, M. Structural Basis of Polydopamine Film Formation: Probing 5,6-Dihydroxyindole-Based Eumelanin Type Units and the Porphyrin Issue. *ACS Appl. Mater. Interfaces* **2018**, *10* (9), 7670−7680.

(56) d'Ischia, M.; Napolitano, A.; Ball, V.; Chen, C.-T.; Buehler, M. J. Polydopamine and Eumelanin: From Structure−Property Relationships to a Unified Tailoring Strategy. *Acc. Chem. Res.* **2014**, *47* (12), 3541−3550.

(57) Zheng, Y.; Huang, Z.; Zhao, C.; Weng, S.; Zheng, W.; Lin, X. A Gold Electrode with a Flower-like Gold Nanostructure for Simultaneous Determination of Dopamine and Ascorbic Acid. *Microchim. Acta* **2013**, *180* (7−8), 537−544.

(58) Yang, Y. X.; Fang, Y. Z.; Tian, J. X.; Xiao, Q.; Kong, X. J. Fluorescent Polydopamine Nanoparticles as a Nanosensor for the Sequential Detection of Mercury Ions and l-Ascorbic Acid Based on a Coordination Effect and Redox Reaction. *RSC Adv.* **2020**, *10* (47), 28164−28170.

(59) Walcarius, A.; Sibottier, E.; Etienne, M.; Ghanbaja, J. Electrochemically Assisted Self-Assembly of Mesoporous Silica Thin Films. *Nat. Mater.* **2007**, *6* (8), 602−608.

(60) Li, Y.; Maire, H. C.; Ito, T. Electrochemical Characterization of Nanoporous Films Fabricated from a Polystyrene-Poly-(Methylmethacrylate) Diblock Copolymer: Monitoring the Removal of the PMMA Domains and Exploring the Functional Groups on the Nanopore Surface. *Langmuir* **2007**, *23* (25), 12771−12776.

(61) Perera, D. M. N. T.; Ito, T. Cyclic Voltammetry on Recessed Nanodisk-Array Electrodes Prepared from Track-Etched Polycarbonate Membranes with 10-Nm Diameter Pores. *Analyst* **2010**, *135* (1), 172−176.

(62) Jaugstetter, M.; Blanc, N.; Kratz, M.; Tschulik, K. Electrochemistry under Confinement. *Chem. Soc. Rev.* **2022**, *51* (7), 2491−2543.

(63) Tom, J. C.; Appel, C.; Andrieu-Brunsen, A. Fabrication and in Situ Functionalisation of Mesoporous Silica Films by the Physical Entrapment of Functional and Responsive Block Copolymer Structuring Agents. *Soft Matter* **2019**, *15*, 8077.

(64) Stanzel, M.; Kunz, U.; Andrieu-Brunsen, A. Layer-Selective Functionalisation in Mesoporous Double Layer via Iniferter Initiated Polymerisation for Nanoscale Step Gradient Formation. *Eur. Polym. J.* **2021**, *156*, No. 110604.

(65) Brunsen, A.; Cui, J.; Ceolín, M.; Campo, A. d.; Soler-Illia, G. J. A. A.; Azzaroni, O. Light-Activated Gating and Permselectivity in Interfacial Architectures Combining "Caged" Polymer Brushes and Mesoporous Thin Films. *Chem. Commun.* **2012**, *48* (10), 1422−1424.

(66) Tagliazucchi, M.; Williams, F. J.; Calvo, E. J. Effect of Acid-Base Equilibria on the Donnan Potential of Layer-by-Layer Redox Polyelectrolyte Multilayers. *J. Phys. Chem. B* **2007**, *111* (28), 8105−8113.

(67) Basnig, D.; Vilá, N.; Herzog, G.; Walcarius, A. Voltammetric Behaviour of Cationic Redox Probes at Mesoporous Silica Film Electrodes. *J. Electroanal. Chem.* **2020**, *872*, No. 113993.

(68) McKenzie, K. J.; King, P. M.; Marken, F.; Gardner, C. E.; MacPherson, J. V. Assembly of Thin Mesoporous Titania Films and Their Effects on the Voltammetry of Weakly Adsorbing Redox Systems. *J. Electroanal. Chem.* **2005**, *579* (2), 267−275.

(69) Calvo, A.; Yameen, B.; Williams, F. J.; Soler-Illia, G. J. A. A.; Azzaroni, O. Mesoporous Films and Polymer Brushes Helping Each Other to Modulate Ionic Transport in Nanoconfined Environments. An Interesting Example of Synergism in Functional Hybrid Assemblies. *J. Am. Chem. Soc.* **2009**, *131* (31), 10866−10868.

(70) Karman, C.; Vilà, N.; Walcarius, A. Amplified Charge Transfer for Anionic Redox Probes through Oriented Mesoporous Silica Thin Films. *ChemElectroChem* **2016**, *3* (12), 2130−2137.

(71) Brinker, C. J.; Lu, Y.; Sellinger, A.; Fan, H. Evaporation-Induced Self-Assembly: Nanostructures Made Easy. *Adv. Mater.* **1999**, *11*, 585−579.

(72) Boissiere, C.; Grosso, D.; Lepoutre, S.; Nicole, L.; Bruneau, A. B.; Sanchez, C. Porosity and Mechanical Properties of Mesoporous Thin Films Assessed by Environmental Ellipsometric Porosimetry. *Langmuir* **2005**, *21* (26), 12362−12371.

(73) Elgrishi, N.; Rountree, K. J.; McCarthy, B. D.; Rountree, E. S.; Eisenhart, T. T.; Dempsey, J. L. A Practical Beginner's Guide to Cyclic Voltammetry. *J. Chem. Educ.* **2018**, *95* (2), 197−206.

(74) Alberti, S.; Steinberg, P. Y.; Giménez, G.; Amenitsch, H.; Ybarra, G.; Azzaroni, O.; Angelomé, P. C.; Soler-Illia, G. J. A. A. Chemical Stability of Mesoporous Oxide Thin Film Electrodes under Electrochemical Cycling: From Dissolution to Stabilization. *Langmuir* **2019**, *35* (19), 6279−6287.